DEPARTMENT OF TRANSPORTATION

Innovative Materials and Advanced Technologies for a Sustainable Pavement Infrastructure

Jia-Liang Le, Principal Investigator
Department of Civil, Environmental, and Geo- Engineering
University of Minnesota

JUNE 2021

Research Project
Final Report 2021-18

LRRB
LOCAL
ROAD RESEARCH
BOARD

Technical Report Documentation Page

1. Report No. MN 2021-18	2.	3. Recipients Accession No.

4. Title and Subtitle Innovative Materials and Advanced Technologies for a Sustainable Pavement Infrastructure	5. Report Date June 2021 6.
7. Author(s) Jia-Liang Le, Mihai Marasteanu, Lawrence Zanko, Jhenyffer Matias de Oliveira, Thomas Calhoon, Mugurel Turos, Tyler Stricherz, David Hopstock, Vern Hegg,	8. Performing Organization Report No.
9. Performing Organization Name and Address Dept. of Civil, Environmental, and Geo- Engineering University of Minnesota, Twin Cities 500 Pillsbury Drive, Minneapolis, MN Natural Resources Research Institute (NRRI) University of Minnesota, Duluth Hopstock and Associates LLC. Microwave Industry Consultant LLC.	10. Project/Task/Work Unit No. CTS# 2019006 11. Contract (C) or Grant (G) No. (c)1003325 (wo)71
12. Sponsoring Organization Name and Address Minnesota Local Road Research Board Minnesota Department of Transportation Office of Research & Innovation 395 John Ireland Boulevard, MS 330 St. Paul, Minnesota 55155-1899	13. Type of Report and Period Covered Final Report 14. Sponsoring Agency Code

15. Supplementary Notes

https://www.mndot.gov/research/reports/2021/202118.pdf

16. Abstract (Limit: 250 words)

It is widely acknowledged that early detection of material damage and timely rehabilitation can lead to a significant reduction in the life-cycle cost of asphalt pavements. This research investigates the capabilities of damage detection and healing of graphite nanoplatelet (GNP)-taconite modified asphalt materials. The first part of the research is concerned with the application of GNP-taconite modified asphalt materials for damage detection using electrical conductivity. It is shown that, as compared to conventional asphalt materials, the GNP-taconite modified asphalt materials exhibit an improved electrical conductivity due to the electron hopping mechanism. Based on the mathematical analogy between the elastostatic field and the electrostatic field, a theoretical model is derived to relate the change of electrical conductivity to the damage extent of the material. Although, in principle, the material damage can be accessed using the electrical conductivity, the practical application of this method is complicated by the fact that the conductivity is influenced by the moisture content. The second part of the research investigates the damage healing capability of GNP-taconite modified asphalt materials heated by microwave. GNP-taconite modified asphalt materials can effectively absorb the heat generated by the microwave, and the rising temperature can effectively heal the microcracks in the binder. This damage-healing mechanism is verified by a set of semi-circular beam tests. Finally, microwave heating technology is applied to the tack coat system. It is shown that, with microwave heating, the GNP-taconite modified asphalt material can effectively improve the bond strength of the interface of the tack coat system.

17. Document Analysis/Descriptors Asphalt based materials, Deterioration, Sensors, Microwave detectors, Graphite, Electrical conductivity	18. Availability Statement No restrictions. Document available from: National Technical Information Services, Alexandria, Virginia 22312

19. Security Class (this report) Unclassified	20. Security Class (this page) Unclassified	21. No. of Pages 75	22. Price

INNOVATIVE MATERIALS AND ADVANCED TECHNOLOGIES FOR A SUSTAINABLE PAVEMENT INFRASTRUCTURE

FINAL REPORT

Prepared by:

Jia-Liang Le
Mihai Marasteanu
Jhenyffer Matias de Oliveira
Thomas Calhoon
Mugurel Turos
Tyler Stricherz
Department of Civil, Environmental, and Geo- Engineering
University of Minnesota, Twin Cities

Lawrence M. Zanko
Natural Resources Research Institute (NRRI)
University of Minnesota, Duluth

David Hopstock
Hopstock and Associates LLC.

Vern Hegg
Microwave Industry Consultant LLC.

JUNE 2021

Published by:

Minnesota Department of Transportation
Office of Research & Innovation
395 John Ireland Boulevard, MS 330
St. Paul, Minnesota 55155-1899

ACKNOWLEDGMENTS

The research team would like to gratefully acknowledge the Minnesota Department of Transportation for its financial support.

The research team would like to thank the members of the Technical Advisory Panel for their guidance in this effort, including Darrick Anderson, Eddie Johnson, James Johnson, Julie Long, Clark Moe, Layne Otteson, Tim Schoonhoven, and Andrew Scipioni. The research team would also like to thank MnDOT's Technical Liaison Juan Pinero and Project Coordinator Elizabeth Klemann.

Special thanks go to Glenn Engstrom and Ben Worel, who supported the idea that there was a critical need for innovation and new materials in pavement applications.

TABLE OF CONTENTS

CHAPTER 1: Introduction 1

1.1 Background 1

1.2 Objective 1

1.3 Organization of the Report 1

CHAPTER 2: Literature Review 3

2.1 Non-Destructive Testing 3

2.1.1 Self-Calibrating Ultrasonic Technique 3

2.1.2 Rolling Density Meter 5

2.1.3 Scanning Laser Detection System 5

2.1.4 Digital Image Correlation System 6

2.2 Benefits of Proactive Pavement Preservation 7

CHAPTER 3: Electrical Conductivity Experiments on GNP-Taconite Modified Asphalt Materials 10

3.1 Previous Work on Electrical Conductivity of GNP-Modified Asphalt Materials 10

3.2 Electrical Conductivity of GNP-Taconite Concentrate Modified Asphalt Materials 15

CHAPTER 4: Derivation of the Relationship Between the Damage Extent and Electrical Resistance 23

4.1 Mathematical Model 23

4.2 Experimental Investigation 27

4.3 Discussion 32

CHAPTER 5: Investigation of Self-Healing Capacity of GNP-Taconite Modified Asphalt Mixtures 34

5.1 Initial Experimental Work 34

5.1.1 Materials and Test Specimen Preparation 34

5.1.2 Preloading Procedure to Induce Partial Damage 35

5.1.3 Healing Procedure Using Microwave Energy 37

5.1.4 Evaluation of Damage and Healing Using CMOD Results 37

5.2 Experimental Testing Using SCB 39

CHAPTER 6: Investigation of a Microwave-Based Tack Coat System to Enhance Interlayer Bonding ... 45

6.1 Specimen Preparation 45

6.2 Microwave Experiments 46

6.3 Tack Bond Shear Strength Testing 49

6.4 Experimental Results and Discussion 50

CHAPTER 7: Research Benefits and Implementation Steps 55

7.1 Research Benefits 55

7.2 Implementation Steps 59

CHAPTER 8: Summary, Conclusion, and Recommendations 60

REFERENCES 62

LIST OF FIGURES

Figure 2.1: Ultrasonic tester UK1401. (Khazanovich *et. al.*, 2005) 3

Figure 2.2: Schematics of test procedure: (a) longitudinal and (b) transverse. (Khazanovich *et. al.*, 2005) 4

Figure 2.3: Ultrasonic tomography device (MIRA) in longitudinal (left) and transverse (right) orientations (set for transverse and longitudinal step sizes, respectively). (Hoegh *et. al.*, 2012) 4

Figure 2.4: Equipment and Data Collection before a 500 ft pass (left), and during data collection moving behind the final roller compactor (right). (Hoegh & Dai, 2017) 5

Figure 2.5: Photograph of laser scanning detection setup. (Ajideh *et. al.*, 2012) 6

Figure 2.6: Setup for Digital Image Correlation system (left). Real image of the lateral surface of a test slab (right) (Bueno & Arraigada, 2016). 6

Figure 2.7: Full-field strain maps during different damage stages. (Bueno & Arraigada, 2016) 7

Figure 2.8: Effects of pavement preservation on pavement condition over time. (Chan *et. al.*, 2011) 8

Figure 2.9: Funding necessary to address WSDOT deferred pavement rehabilitation. (Uhlmeyer *et. al.*, 2016) 9

Figure 3.1: Four-point probe setup. 10

Figure 3.2: (a) Mold preparation; (b) beam cured with four electrodes. 11

Figure 3.3: Average voltage for (a) PG 58-28 with 850 GNP and (b) PG 58-28 with 4827 GNP. 14

Figure 3.4: Conductivity for (a) PG 58-28 with 850 GNP and (b) PG 58-28 with 4827 GNP. 14

Figure 3.5: Taconite concentrate size distributions 15

Figure 3.6: Sample with copper electrodes immediately after pouring. 16

Figure 3.7: Four-probe conductivity test: (a) semiconductor device analyzer, and (b) four-probe measurement setup. 17

Figure 3.8: Applied current vs. voltage and resistance for sample number 1 from: (a) test 1 (b) test 2. .. 17

Figure 3.9: Applied current vs. voltage and resistance for sample number 2 from: (a) test 1 (b) test 2. .. 18

Figure 3.10: Applied current vs. voltage and resistance for sample number 3 from: (a) test 1; (b) test 2. 18

Figure 3.11: Applied current vs. voltage and resistance for sample number 4 from: (a) test 1; (b) test 2. 19

Figure 3.12: Average resistance of the eight measurements. 20

Figure 3.13: Resistivity of the eight measurements. 20

Figure 3.14: Conductivity of the eight measurements. 21

Figure 4.1: A damaged specimen with notch length a: (a) crack detection with conductive plates attached to the ends of the specimen; (b) mathematical analogy of anti-plane shear applied to the ends of the specimen. 24

Figure 4.2: Streamlines flowing through a specimen with a finite notch width. 26

Figure 4.3: Sample preparation: beam molds with four copper electrodes. 27

Figure 4.4: Sample preparation: foil film holding the notch. 28

Figure 4.5: Four-probe measurement setup. 28

Figure 4.6: Applied current vs. voltage and resistance for: (a) sample 1 and (b) sample 2 29

Figure 4.7: Applied current vs. voltage and resistance for: (a) sample 3 and (b) sample 4 29

Figure 4.8: Applied current vs. voltage and resistance for: (a) sample 5 and (b) sample 6 30

Figure 4.9: Average resistance of the six measurements 31

Figure 4.10: Resistivity of the six measurements 31

Figure 4.11: Conductivity of the six measurements 32

Figure 5.1: Asphalt mixture specimen. 34

Figure 5.2: Axial displacement vs time. 36

Figure 5.3: A sine waveform was used in testing the specimens. 37

Figure 5.4a: Measured CMOD amplitude over cycles. 38

Figure 5.4b: Measured CMOD amplitude over cycles. 38

Figure 5.4c: Measured CMOD amplitude over cycles. 39

Figure 5.4d: Measured CMOD amplitude over cycles. 39

Figure 5.5: Comparison of peak loads, 80% post-peak loads, and final fracture loads. 41

Figure 5.6: Experimental results on the mixture with 6% GNP not microwaved (NON). 43

Figure 5.7: Experimental results on the mixture with 6% GNP and 1% taconite concentrate microwaved. 44

Figure 6.1: Bottom pucks with applied tack coat. 46

Figure 6.2: Specimen setup for determining microwave heating duration: (a) Diagram of the specimen, (b) Specimen held by wooden jigs, (c) Specimen voltage being read 47

Figure 6.3: Microwave setup used to heat the GNPC specimens: (a) full setup and (b) close-up........ 48

Figure 6.4: Pre- and post-microwaved thermal images of the specimen........ 48

Figure 6.5: MS-43 Asphalt Tack Bond Shear Strength Apparatus........ 49

Figure 6.6: A specimen that failed along the tack coat interface. 50

Figure 6.7: Results of the GNPC specimen tack coat shear strength tests at room temperature........ 51

Figure 6.8: Results of the control specimen tack coat shear strength tests at room temperature. 51

Figure 6.9: Results of the GNPC specimen tack coat shear strength tests at refrigerator temperature........ 52

Figure 6.10: Results of the control specimen tack coat shear strength tests at refrigerator temperature. 52

Figure 6.11: Results of the GNPC specimen tack coat shear strength tests at freezer temperature........ 53

Figure 6.12: Results of the control specimen tack coat shear strength tests at freezer temperature........ 53

Figure 6.13: Average of the max shear stress readings for tests within each temperature grouping in the two sets........ 54

Figure 7.1: Control pavement structure for TH-5 56

Figure 7.2: Maintenance schedule for mill and overlay. 57

Figure 7.3: Modified maintenance schedule for mill and overlay. 58

Figure 7.4: Comparison of annual equivalent costs over 35 years 59

LIST OF TABLES

Table 3.1: Description of GNP materials........ 10

Table 3.2: Samples investigated in IDEA project........ 12

Table 3.3: Results from conductivity tests performed on samples mixed with high shear rate. 12

Table 3.4: Average resistance, resistivity, and conductivity results. 13

Table 3.5: Mix designs used in the GNP-concentrate experiments........ 16

Table 3.6: Average resistance, resistivity, and conductivity results. 19

Table 4.1: Mix designs and notch sizes used in the GNP-concentrate notched samples. 27

Table 4.2: Average resistance, resistivity, and conductivity results. 30

Table 4.3: Dielectric values air, water, ice, and different subgrade soils and road materials (Saarenketo, 2006) 33

Table: 5.1: Results from the Strength Tests to Failure. 35

Table 5.2: SCB Test Results. 42

Table 5.3: Fracture load to post-peak load ratios. 43

Table 6.1: 15-minute heating record of nine GNPC specimens, January 5, 2021. 49

Table 6.2: Average max shear stress and standard deviation 54

Table 7.1: Key expected benefits 55

Table 7.2: Initial costs for placement of one mile of mill and overlay (control) 56

EXECUTIVE SUMMARY

It is widely acknowledged that early detection of material damage and timely rehabilitation can lead to a significant reduction in life-cycle cost of asphalt pavements. This research investigates the capabilities of graphite nanoplatelet (GNP)-taconite modified asphalt materials in damage detection and healing. The first part of the research is concerned with the application of GNP-taconite modified asphalt materials for damage detection using electrical conductivity. It is shown that, as compared to conventional asphalt materials, GNP-taconite modified asphalt materials exhibit improved electrical conductivity. This improvement can be attributed to the enhancement of the electron hopping mechanism by the GNP and taconite. Based on the mathematical analogy between the elastostatic field and the electrostatic field, a theoretical model is derived to relate the change of electrical conductivity to the damage extent of the material. Although, in principle, the material damage can be accessed by using electrical conductivity, the practical application of this method is complicated because the conductivity is influenced by moisture content.

The second part of the research investigates the damage healing capability of GNP-taconite modified asphalt materials after microwave heating. GNP-taconite modified asphalt materials can effectively absorb the heat generated by the microwave, and the rising temperature can effectively heal the microcracks in the binder. This damage healing mechanism is then verified by a set of semi-circular beam tests. Finally, microwave heating technology is applied to the tack coat system. It is shown that, with microwave heating, the GNP-taconite modified asphalt material can effectively improve the bond strength of the interface of the tack coat system.

CHAPTER 1: INTRODUCTION

1.1 BACKGROUND

It is widely accepted that early detection of material damage and timely repair would lead to a significant reduction in life-cycle cost of pavement infrastructure. Motivated by this concept, extensive efforts have been devoted toward innovative non-destructive techniques of damage detection. However, most of these techniques rely on advanced devices and equipment, which sometimes are not easily accessible. Meanwhile, cost-efficient repair of asphalt pavements also represents a major challenge. Repair material often possesses different properties as compared to the original material, which can cause stress concentration. Furthermore, during the early stage, damage appears in the form of microcracking. Many of these microcracks form inside the pavement, which makes repair difficult.

Similar challenges also exist in other infrastructure materials, such as concrete. Recent attention has been directed toward developing innovative materials, which can be used for damage sensing and healing. Such concepts are appealing since self-sensing and healing materials will significantly reduce the cost of damage detection and repair. However, a very limited number of studies have been conducted on developing self-sensing and healing asphalt materials. This research aims to fill this knowledge gap.

1.2 OBJECTIVE

This research aims to investigate the damage sensing and healing capabilities of graphite nano-platelet (GNP)-taconite modified asphalt materials. The damage sensing mechanism is anchored by a mathematical model between the change of electrical conductivity and the extent of damage. To utilize this relationship, four-probe experiments are performed to examine the improvement of the electrical conductivity of GNP-taconite modified asphalt materials. Subsequent electrical conductivity tests are performed on specimens with differing pre-existing damage to further verify the proposed concept. The damage healing mechanism is based on the heat generation of microwaving. To this end, a set of healing experiments are performed on pre-damaged semi-circular bend beams. These tests are used to examine the level of recovery of load capacity of the specimen after microwaving. Meanwhile, the concept of microwave heating is also applied to enhance the interfacial bond strength of the tack coat system.

1.3 ORGANIZATION OF THE REPORT

First, a literature review is performed to give a summary of the current state of non-destructive asphalt condition testing. Several non-destructive types of equipment and methods used to measure damage in asphalt pavements are discussed. Many of these act as in-field alternatives to laboratory testing methods. Methods are highlighted that can measure delamination, evaluate visible cracks, measure air void content, monitor and characterize fatigue behavior, and evaluate strength recovery. The literature review also highlights the benefits of well-timed proactive pavement preservation and the detriments of deferred maintenance. The methods used by several states to tackle this issue are explored. This includes a discussion of novel condition parameters and a case study that compares the consequences of different pavement preservation approaches. The fiscal and environmental costs of delaying proper preservation are also discussed.

A series of experiments are performed to measure the conductivity and resistivity of GNP and taconite concentrate modified asphalt binders. Previous work performed with GNP addition to binders is discussed. This work informs the mix and preparation methods used in the mentioned experiments. Asphalt binder specimens are created with varying added amounts of GNP and taconite concentrate. The method used to measure the conductivity and resistivity within the specimens is discussed, then the results of these experiments are presented. The results are analyzed along with theory on improving the electrical conductivity within binder mixes. An optimal mix of GNP and taconite concentrate within the binder is decided on, and then that mix is used in the subsequent tests performed in this study.

The relationship between damage extent in the binder and electrical conductivity and resistance is explored. A mathematical model is derived to measure that relationship. The model is crafted using the analogous relationship between the solution of a 2D electrostatic field and the solution of a 2D elastostatic field under anti-plane shear loading. The analogy is fully considered and discussed. Tests are then performed to measure the effect of applying controlled damage (notches) to a binder specimen on the electrical conductivity of the specimen. The GNP-taconite asphalt binder mix used in the previous section is used for these tests. Specimen preparation and testing procedures are outlined, and results are presented then discussed.

A set of laboratory experiments is performed to investigate the damage healing capacity of GNP-taconite modified asphalt mixtures. Asphalt mixture specimens are first loaded to the post-peak regime to induce a certain level of damage. These pre-damaged specimens are then subjected to microwave for a short duration and are reloaded again to ultimate failure. The comparison between the load-deflection responses of the first and second loading is used to examine the healing capability.

Finally, the effects of exposing a GNP-taconite modified tack coat to microwave energy on the interlayer bond shear strength of the tack coat is investigated. The specimen preparation, microwave application, and shear strength testing processes are fully explained. The test results are presented and discussed and calls for further investigation are made.

CHAPTER 2: LITERATURE REVIEW

In this chapter, a summary of current knowledge and practice of non-destructive testing of asphalt pavements, as well as the benefits of proactive pavement preservation methods, is presented.

2.1 NON-DESTRUCTIVE TESTING

Laboratory testing methods, such as fatigue testing in tension/compression, bending and complex modulus testing, are routinely used to evaluate damage occurrence in pavement materials under various loading conditions. This is done by analyzing how specific material properties change with time under static or repeated loading. This option is not available to detect and assess damage in pavement structures in the field. In this particular case, non-destructive methods are needed. A literature search found several methods available for this purpose. A summary of non-destructive tests that can be used to detect crack initiation and healing in asphalt concrete pavement is presented below.

2.1.1 Self-Calibrating Ultrasonic Technique

An ultrasonic technology that has been used successfully for many years to determine cracking in concrete structures, provided an evaluation of distresses in asphalt concrete pavements through a simple procedure. (Khazanovich *et. al.*, 2005) The ultrasonic tester, a UK1401 (Figure 2.1), is used to obtain crack measurements in two directions: along and across each crack.

Figure 2.1: Ultrasonic tester UK1401. (Khazanovich *et. al.*, 2005)

The device measures the velocity of signal propagation and calculates the wave velocity. Figure 2.2 shows a schematic representation of the test procedure. (Khazanovich *et. al.*, 2005) The advantages of the method include an easy-to-operate portable device, no surface preparation or local calibration required, and straightforward results. More research is needed before recommending the procedure for routine use in pavement evaluation.

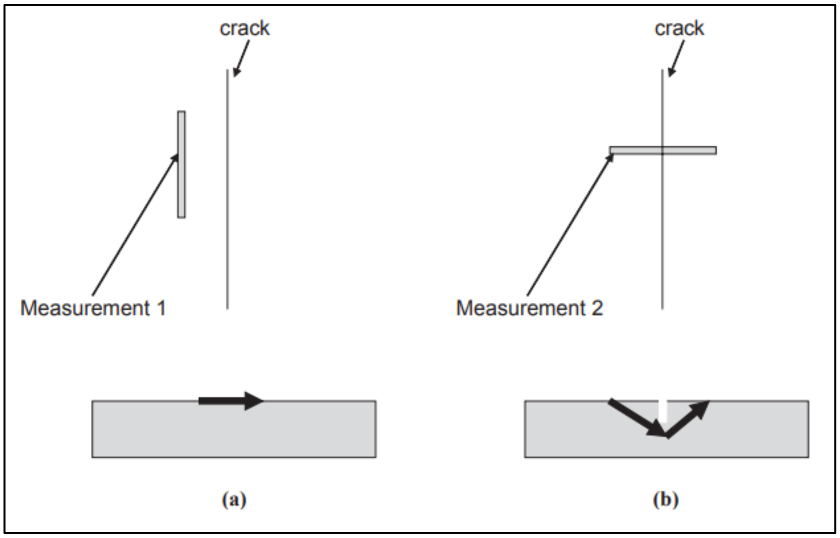

Figure 2.2: Schematics of test procedure: (a) longitudinal and (b) transverse. (Khazanovich *et. al.*, 2005)

A more advanced system has been recently used to detect delamination in asphalt pavements. MIRA, an ultrasonic tomography device shown in Figure 2.3, is capable to detect the type and severity of delamination before the visual appearance of the pavement distress. (Hoegh *et. al.*, 2012)

An image of two ultrasonic tomography devices with yellow handle, each placed in a different direction of traffic.

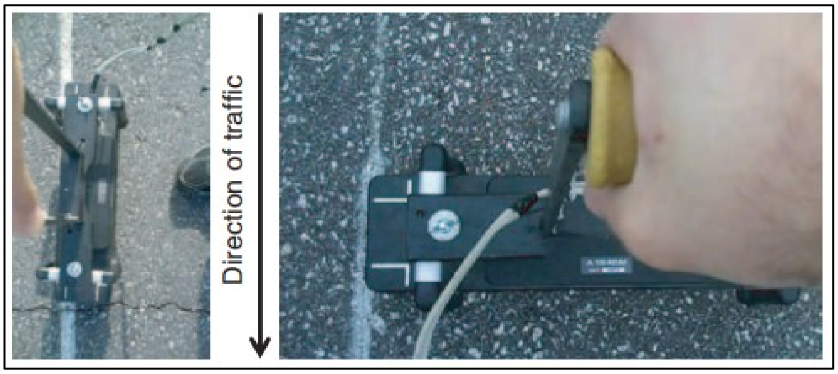

Figure 2.3: Ultrasonic tomography device (MIRA) in longitudinal (left) and transverse (right) orientations (set for transverse and longitudinal step sizes, respectively). (Hoegh *et. al.*, 2012)

MIRA generates a two-dimensional depth profile of the subsurface under the measurement location through a system of 45 transmitting and receiving channel pair measurements, with four transducers in each channel. Blind tests performed at the NCAT test track in Auburn, Alabama have shown MIRA can detect delamination at the interface between old and new asphalt layers.

2.1.2 Rolling Density Meter

Pavement performance is highly affected by air void content (Linden *et. al.*, 1989). It is estimated that each 1 percent of air void increase (after 7 percent) results in 10 percent pavement deterioration (Linden *et. al.*, 1989). As a result, the quality of compaction is crucial to pavement performance. This enhances the need for non-destructive tests that can be used in compaction quality control.

The Rolling Density Meter (RDM), which is a Ground-penetrating radar (GPR), provides a non-destructive alternative to evaluate asphalt pavement air voids. The RDM, shown in Figure 2.4, is a commercially available device recently developed under an SHRP2 study that can be used to assess relative compaction levels nondestructively. (Hoegh & Dai, 2017)

Figure 2.4: Equipment and Data Collection before a 500 ft pass (left), and during data collection moving behind the final roller compactor (right). (Hoegh & Dai, 2017)

RDM provides data that can be cross-checked with other data and used to determine the most critical factors in achieving proper compaction. The RDM information can also be used for quality assurance of as-built compaction uniformity and assessment of in-place compaction spatial variation. The results are provided as histograms, heat maps, scatter plots, and general statistics. (Hoegh & Dai, 2017)

2.1.3 Scanning Laser Detection System

Scanning laser detection, also known as SLD, is used to monitor damage and characterize fatigue behavior of asphalt mixtures. As shown in Figure 2.5, a laser beam sweeps the specimen surface at a constant frequency. The data is recorded and analyzed by a computer-controlled measuring system and used to calculate the defect frequency (DF) parameter.

Figure 2.5: Photograph of laser scanning detection setup. (Ajideh *et. al.*, 2012)

The SLD system can detect small cracks, crack initiation, and microcracks spread in specimen surface; crack initiation is captured at earlier stages when compared to traditional methods. The system also generates fatigue performance results that strongly correlate with change in fatigue behavior and mechanical and viscoelastic properties obtained from traditional dissipated energy approaches. Scanning laser detection does not require image processing, resulting in less processing time and memory requirements. (Ajideh *et. al.*, 2012)

2.1.4 Digital Image Correlation System

An optical technique based on digital image correlation (DIC) was used to monitor damage and to evaluate strength recovery during mechanical loading and healing. The procedure involves two digital cameras that record the slab deformation with high accuracy. The left and right images are correlated to provide information about the geometry and position of each point. Figure 2.6 shows the device setup and the slab image generated. (Bueno & Arraigada, 2016)

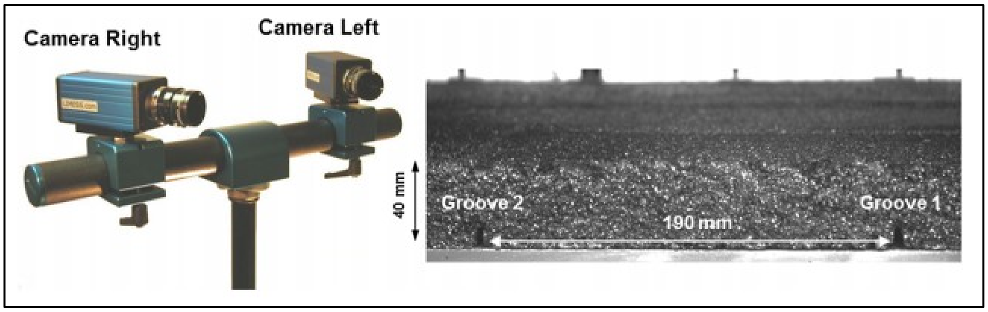

Figure 2.6: Setup for Digital Image Correlation system (left). Real image of the lateral surface of a test slab (right) (Bueno & Arraigada, 2016).

Using this procedure, researchers were able to detect damage accumulation and crack initiation before crack damage was visible, as shown in Figure 2.7. This was an important step since it indicated when to stop the test before damage reached an irreversible level.

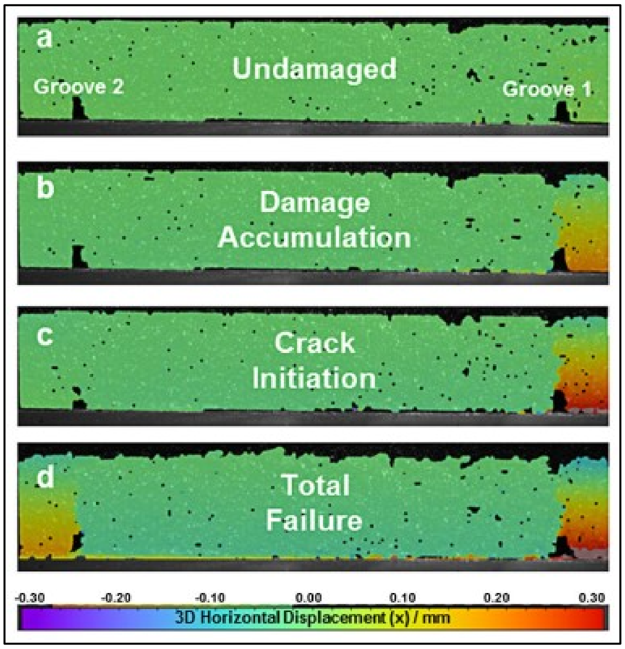

Figure 2.7: Full-field strain maps during different damage stages. (Bueno & Arraigada, 2016)

The slabs were first damaged and then subjected to induction heating. To enhance the heating effect, cast iron particles were added to the slabs subjected to induction heating through an alternating electromagnetic field. The DIC system was able to monitor the accumulated damage and detect crack initiation. The system also monitored the healing of specimens. (Bueno & Arraigada, 2016)

2.2 BENEFITS OF PROACTIVE PAVEMENT PRESERVATION

Pavement preservation can be defined as the use of strategies and treatments performed while the pavement is in good condition, aiming to extend its service life (Chan *et. al.*, 2011). The period to apply preservation treatments is crucial to the effectiveness of preservation treatments. If preservation is done too early, the material will be wasted (Uhlmeyer *et. al.*, 2016). On the other hand, if the treatments are applied too late and the damages are beyond the surface, the road might need to be subjected to rehabilitation or reconstruction instead, resulting in far higher costs for agencies and users (Uhlmeyer *et. al.*, 2016). Figure 2.8 shows the extension of the pavement life through pavement preservation, as well as the postponing of more costly interventions. (Chan *et. al.*, 2011)

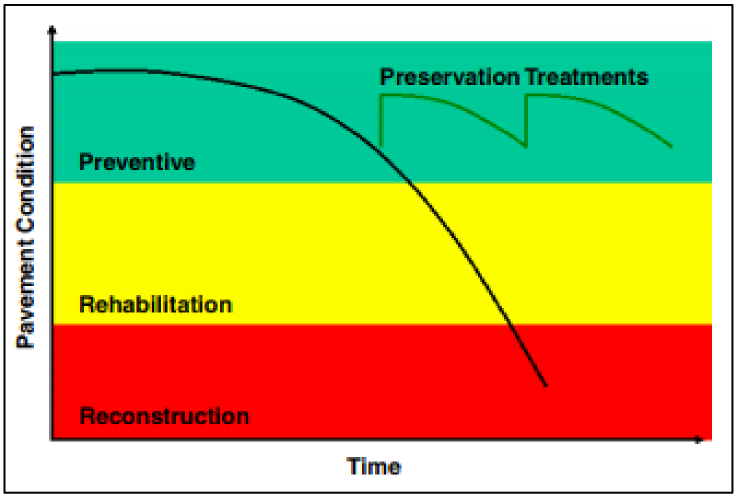

Figure 2.8: Effects of pavement preservation on pavement condition over time. (Chan *et. al.*, 2011)

Some of the most used pavement preservation treatments are crack sealing, slurry seal, microsurfacing, chip seal, ultrathin bonded friction course, fiber-modified chip seal, hot-mix patching, and hot in-place recycling (Chan *et. al.*, 2011). The benefits of pavement preservation include sustainability, less disruption, less contract administration required, fewer greenhouse gas emissions, less energy consumption, and lower agency and use costs.

A case study performed in Canada revealed that environmental benefits from pavement surface maintenance can range from $700,000 to $18,000,000 over a 40 year analysis period. The study analyzed the life cycle environmental benefits of three different preventive practices applied to a one-kilometer road section at the beginning of its service life. The first two preventive practices were a mill and overlay treatment with different trigger values, while the third preventive practice was a seal coat application every 10 years (Pellecuer *et. al.*, 2014). Among the environmental benefits assessed in the study were air pollution, greenhouse gases, and noise. The researchers concluded that the reduction of greenhouse gases emission was relatively small, but noise benefits were surprisingly significant. It was also shown that preventive practices were more effective in mitigating environmental impacts in the long term than corrective treatments, proving that preventive maintenance was more sustainable than corrective maintenance (Pellecuer *et. al.*, 2014).

If deferred funding causes rehabilitation to be postponed to the point where reconstruction is required, the cost difference can be up to several million dollars. The cost to maintain pavement increases as the structure ages and passes the optimum time for rehabilitation. Properly applied preventive practices result in lower replacement cost and better asset conditions (Hammond, 2013).

In a recent research effort related to pothole prevention and innovative repair, the authors found that key components to delay or prevent the formation of potholes are an efficient data tracking system and the use of the right treatment for the right situation at the right time. Such actions are the core of proactive pavement preservation practiced by lead states, such as Washington and Minnesota. (Ghosh *et. al.*, 2018)

WSDOT introduced the Deferred Preservation Liability as a new performance measure aiming to improve the evaluation of pavement preservation needs and it is used to estimate the cost in current dollars to address the cumulative agency cost of past due pavement rehabilitation work (Uhlmeyer *et. al.*, 2016). Deferred Preservation Liability is calculated based on average resurfacing costs for chip seal and asphalt, average triage cost of concrete (dowel bar retrofit and diamond grinding), average cost of concrete reconstruction, distribution of Preservation Unit Due Years, and the Due Year used to start accumulating liability. Currently, the Due Year is 2 years before the year being reported, for instance, the 2012 report only took into consideration Preservation Units due in 2010 and prior. Figure 2.9 shows the number of dollars in millions required to address all WSDOT deferred pavement rehabilitation.

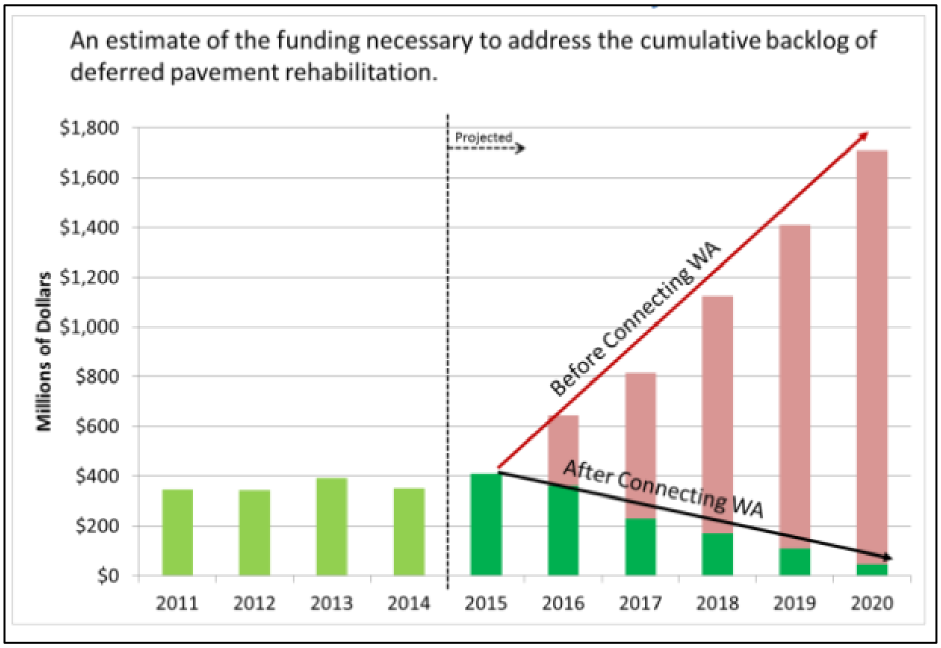

Figure 2.9: Funding necessary to address WSDOT deferred pavement rehabilitation. (Uhlmeyer *et. al.*, 2016)

Deferred Preservation Liability increases with lack of funding and gets worse as pavement ages (Hammond, 2013). Asset Sustainability Ratio is defined as the ratio between how much life is added to the system versus how much life is consumed in the same year. The ratio makes it possible to monitor how well the management strategies are keeping up with pavement wear (Uhlmeyer *et. al.*, 2016). The Asset Sustainability Ratio target is 1.0, a perfect situation in which the same amount of service life consumed is being replaced. If the ratio is less than 1.0, more lane miles of pavement are being consumed by aging than lane mile years are being put into the system. (Hammond, 2013)

As pavement ages, damages get more severe, resulting in a more costly repair than it would have been if the needs were addressed earlier. The increase of Deferred Preservation Liability usually matches the decrease in Remaining Service Life and Asset Sustainability Ratio, reflecting a deterioration trend that will cause a more costly rehabilitation in the future. (Hammond, 2013)

CHAPTER 3: ELECTRICAL CONDUCTIVITY EXPERIMENTS ON GNP-TACONITE MODIFIED ASPHALT MATERIALS

The research team performed four-probe electrical conductivity experiments on four GNP-taconite modified asphalt materials. Previous work performed on the electrical conductivity of GNP-modified asphalt materials is summarized. In the previous and current experimental work, two types of GNP materials are used, as shown in Table 3.1:

Table 3.1: Description of GNP materials.

GNP type	Description	Carbon content (%)	Surface area (m^2/g)
M850	Graphite nano-flake powder	99.54	13
4827	Surface-enhanced synthetic graphene material	99.66	250

3.1 PREVIOUS WORK ON ELECTRICAL CONDUCTIVITY OF GNP-MODIFIED ASPHALT

The first experiments on measuring the electrical conductivity of asphalt materials modified with graphite nano-platelets were performed as part of an NCHRP IDEA project (Le *et. al.*, 2016). To measure the conductivity of the materials in the beams, the four-point probe method was followed. A schematic of the four-point probe setup is shown in Figure 3.1.

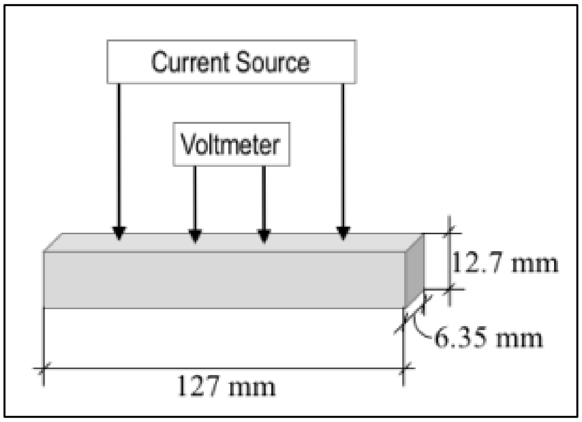

Figure 3.1: Four-point probe setup.

In this first investigation, a Keithley 2401 Source meter was used to apply a constant direct current to the outer two electrodes, and a FLUKE multimeter was used to measure the potential difference between the two inner electrodes. Four different amounts of direct current were applied (0.01 mA, 0.1 mA, 1 mA, and 10 mA).

The samples used for testing were obtained by pouring hot, liquid asphalt material into a Bending Beam Rheometer (BBR) mold that is 5” long, 1/2” tall, and 1/4” thick. Four electrodes made from aluminum screening were placed in the mold before pouring the hot binder such that the distance between the electrodes was 1”. After pouring, the materials were kept in the molds for one hour, then were demolded and stored in the refrigerator. Examples of the setup before pouring and of the demolded sample used for testing are shown in Figure 3.2.

(a) (b)

Figure 3.2: (a) Mold preparation; (b) beam cured with four electrodes.

Two types of asphalt binders, one type of asphalt emulsion, and two GNP materials were used. The binders and GNP were heated at 150°C then were mixed using four different methods:

- Method A: the GNP and binder were mixed by hand for 15 minutes.
- Method B: covering a can containing the binder and GNP with hot sand and keeping it on a vibrating flat lap for 30 minutes.
- Method C: stir the binder and GNP for 15 minutes using a paint mixer.
- Method D: hand-mixed GNP with an asphalt emulsion.

Table 3.2 summarizes the experimental work performed. For this initial batch of experiments, the multimeter did not detect any potential difference, and it was concluded that either GNP reinforced asphalt binders are not electrically conductive, or the mixing method used may not be sufficiently efficient to create a homogeneous dispersion of GNP to increase conductivity.

Table 3.2: Samples investigated in IDEA project

Sample preparation method	Binder type	Percent and type of GNP materials				
		0%	1.50%	3%	6%	10%
A	PG 52-34	--	M850 4827	M850 4827	M850 4827	M850 4827
A	PG 64-34	--	M850 4827	M850 4827	M850 4827	M850 4827
B	PG 52-34	--		M850 4827	M850 4827	
B	PG 64-34	--		M850 4827	M850 4827	
C	PG 52-34	X		M850 4827	M850 4827	
C	PG 64-34	X		M850 4827	M850 4827	
D	Emulsion	X		M850 4827	M850 4827	

In a follow-up experimental work conducted as part of a MnDOT project (Le *et. al.*, 2017), one asphalt binder and two GNP materials were used. In this investigation, the materials were mixed using two methods: hand mixing, as previously done, and using a high shear rate mixer. The same sample preparation and conductivity measuring methods were used in this work. The results, presented in Table 3.3, show that for the samples mixed with the high shear rate mixer, a potential difference of 2.8 to 3.8 mV was measured, while for the samples mixed by hand no voltage was measured. This indicates the shear mixing technique appears to be more efficient at dispersing the GNP materials than hand mixing.

Table 3.3: Results from conductivity tests performed on samples mixed with high shear rate.

GNP type	GNP (%)	Voltage (V)	Resistance (Ohm)	Resistivity (Ohm*m)	Conductivity (mS/m)
4827	3	2.86E-03	2.86E+07	9.23E+04	1.08E-02
4827	6	3.00E-03	3.00E+07	9.68E+04	1.03E-02
M850	3	3.16E-03	3.16E+07	1.02E+05	9.81E-03
M850	6	3.83E-03	3.83E+07	1.24E+05	8.09E-03

Encouraged by the positive results, additional experiments were performed (Kluthe, 2017) using the following materials and mixing method:

- One asphalt binder: unmodified PG58-28
- Two types of GNP: M850 and 4827
- Four compositions: control binder plus 2, 4, 6, and 8% GNP
- Three mixing times at similar mixing temperatures using a high-shear mixer: 15, 30, and 45 minutes.

The same four-point probe method was used to determine the conductivity of the samples: a current source was used to apply 0.3μA and a multimeter was used to measure the voltage. The results are summarized in Table 3.4.

Table 3.4: Average resistance, resistivity, and conductivity results.

Mixing Time (min)	GNP (%)	PG 58-28 with 850 GNP			PG 58-28 with 4827 GNP		
		Average Voltage (V)	Resistivity (Ohm*m)	Conductivity (mS/m)	Average Voltage (V)	Resistivity (Ohm*m)	Conductivity (mS/m)
15	2	4.00E-01	3.84E+03	2.60E-01	4.00E-01	3.84E+03	2.60E-01
30	2	4.00E-01	3.84E+03	2.60E-01	3.33E-01	3.20E+03	3.13E-01
45	2	3.67E-01	3.52E+03	2.84E-01	3.67E-01	3.52E+03	2.84E-01
15	4	4.67E-01	4.48E+03	2.23E-01	5.33E-01	5.12E+03	1.95E-01
30	4	3.67E-01	3.52E+03	2.84E-01	3.00E-01	2.88E+03	3.47E-01
45	4	5.00E-01	4.80E+03	2.08E-01	6.67E-01	6.40E+03	1.56E-01
15	6	6.00E-01	5.76E+03	1.74E-01	5.00E-01	4.80E+03	2.08E-01
30	6	3.00E-01	2.88E+03	3.47E-01	5.33E-01	5.12E+03	1.95E-01
45	6	4.33E-01	4.16E+03	2.40E-01	4.00E-01	3.84E+03	2.60E-01
15	8	3.33E-01	3.20E+03	3.13E-01	6.00E-01	5.76E+03	1.74E-01
30	8	4.00E-01	3.84E+03	2.60E-01	4.67E-01	4.48E+03	2.23E-01
45	8	3.00E-01	2.88E+03	3.47E-01	5.00E-01	4.80E+03	2.08E-01

The potential difference and conductivity results are also summarized in Figures 3.3 and 3.4, respectively. The conductivity values have increased compared to the results from the previous experiments. However, these values are still very low, and, in some cases, the results are quite variable.

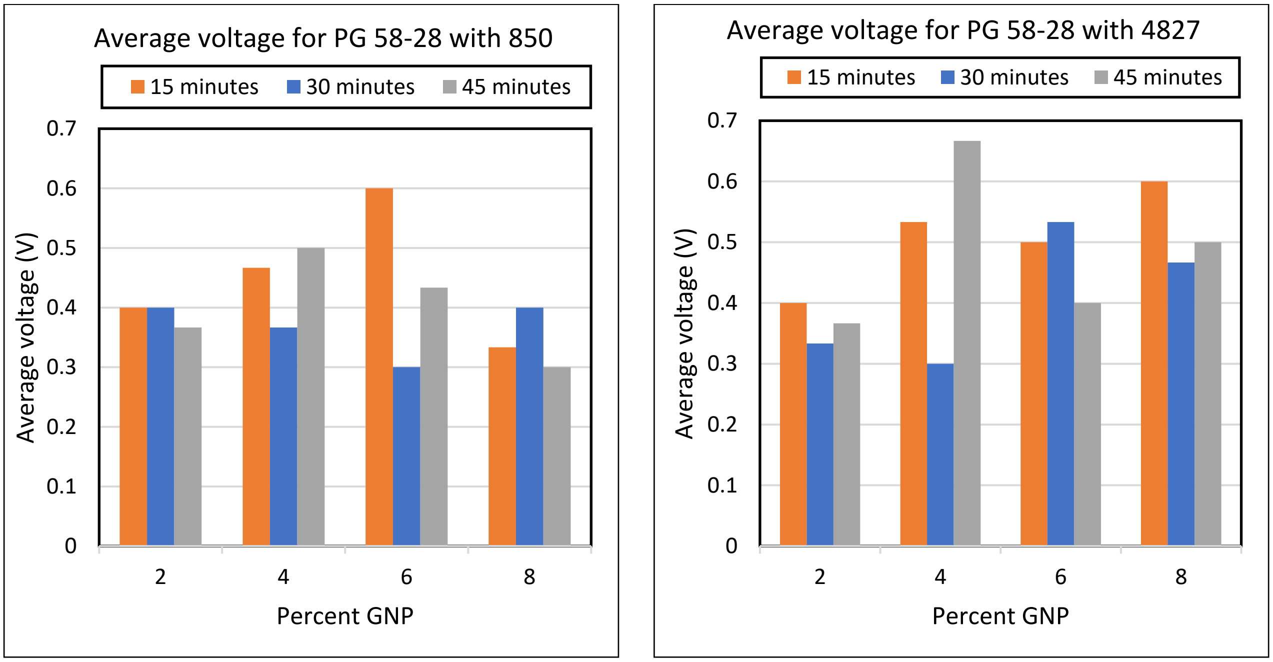

(a) (b)

Figure 3.3: Average voltage for (a) PG 58-28 with 850 GNP and (b) PG 58-28 with 4827 GNP.

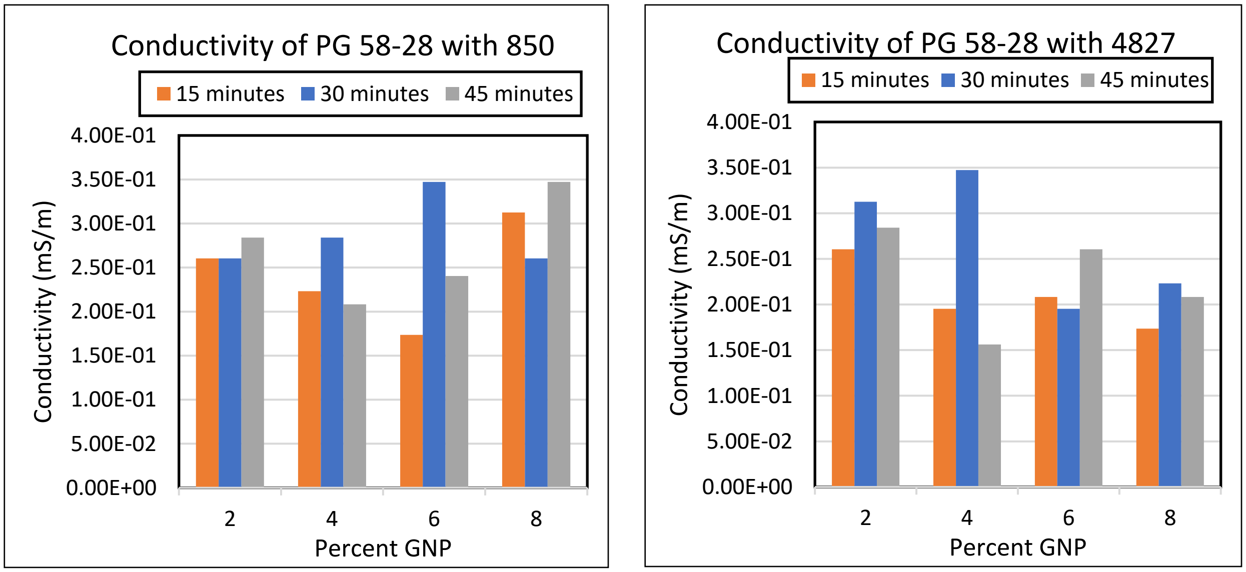

(a) (b)

Figure 3.4: Conductivity for (a) PG 58-28 with 850 GNP and (b) PG 58-28 with 4827 GNP.

To further improve conductivity, it was decided to add small amounts of taconite concentrate to the GNP-modified asphalt materials. In addition, a much more advanced measuring system, used in research on semiconductors, was used to obtain more accurate and consistent results.

3.2 ELECTRICAL CONDUCTIVITY OF GNP-TACONITE CONCENTRATE MODIFIED ASPHALT

The Natural Resources Research Institute at University of Minnesota Duluth provided the concentrate used in this set of experiments. The concentrate produced by the taconite operations typically contains 65% to 66% Fe, mostly as magnetite, before the addition of flux material. Depending on the source operation, the concentrate's silica content can range from 4-7%. All of the operations produce a flux pellet (powdered dolomitic limestone is added as a fluxing agent but in varying percentages). The flux content for three of the operations in Northern Minnesota are as follows:

- 5.75% for ArcelorMittal
- 0.60% for Keetac
- 4.20% for Minntac; Minntac also produces an acid concentrate, which contains no flux.

Figure 3.5 shows the concentrate size distributions for the three operations mentioned above.

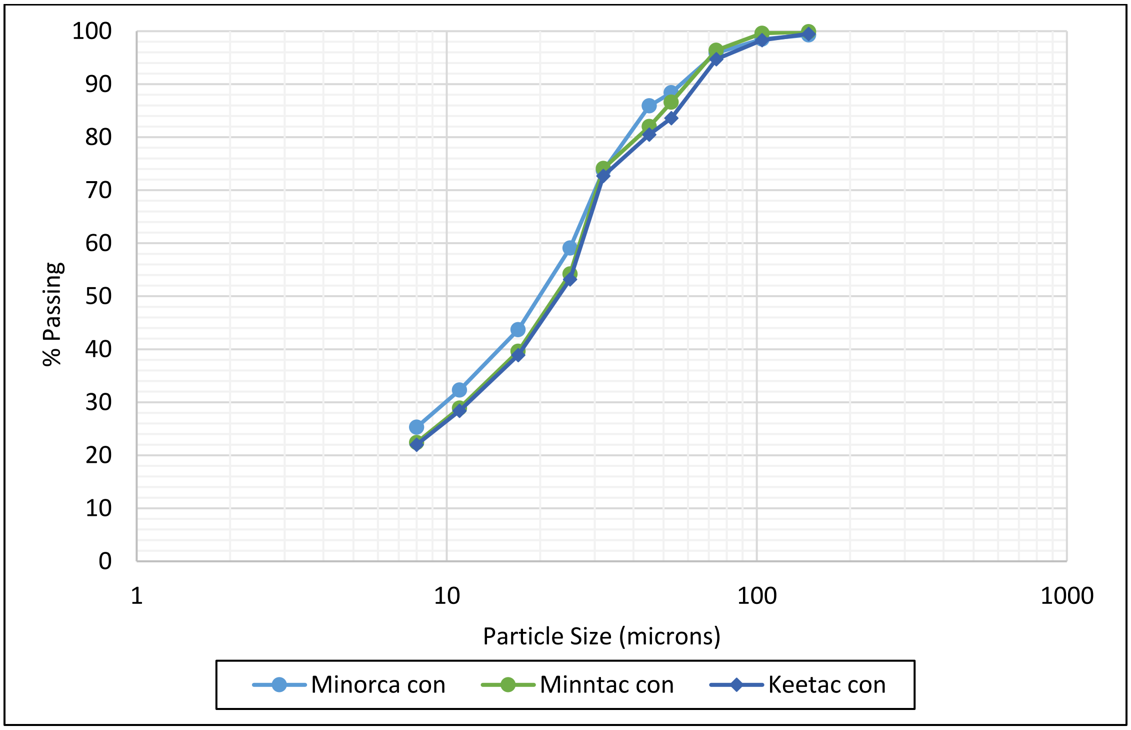

Figure 3.5: Taconite concentrate size distributions

In this set of experiments, flux concentrate from ArcelorMittal (Minorca) and surface-enhanced synthetic graphene material 4827 were used to produce the four mix designs shown in Table 3.5.

Table 3.5: Mix designs used in the GNP-concentrate experiments

Sample No.	Mix Design
1	Control
2	Control + 6% Taconite Concentrate
3	Control + 6% GNP 4827
4	Control + 6% Taconite Concentrate + 6% GNP 4827

The GNP 4827 and heated binder were mixed by a high-velocity shear mixing device for one hour. Due to particle size, the taconite concentrate was mixed with the heated binder through hand stirring for about 5 minutes. The four samples were poured into the beam molds used for BBR experiments. Four electrodes made of copper were placed in the mold and the heated binder was poured, as shown in Figure 3.6. The beams were kept in the refrigerator for 19 days, after which they were tested. The electrical conductivity tests were performed on the four binder beams using the same method as before: the outer two probes were used to supply electrical current to the specimens, while the inner probes were used to measure the voltage.

Figure 3.6: Sample with copper electrodes immediately after pouring.

A semiconductor device analyzer Agilent Technologies B1500A (Figure 3.7) was used to apply a current sweep, which increased in steps from 0 to 10 μA, and to measure the corresponding voltage at each step. As a result, the resistance was calculated for a range of current and voltage values. The outer electrodes shown in Figure 3.7 were used to apply the current and the inner ones, to measure voltage.

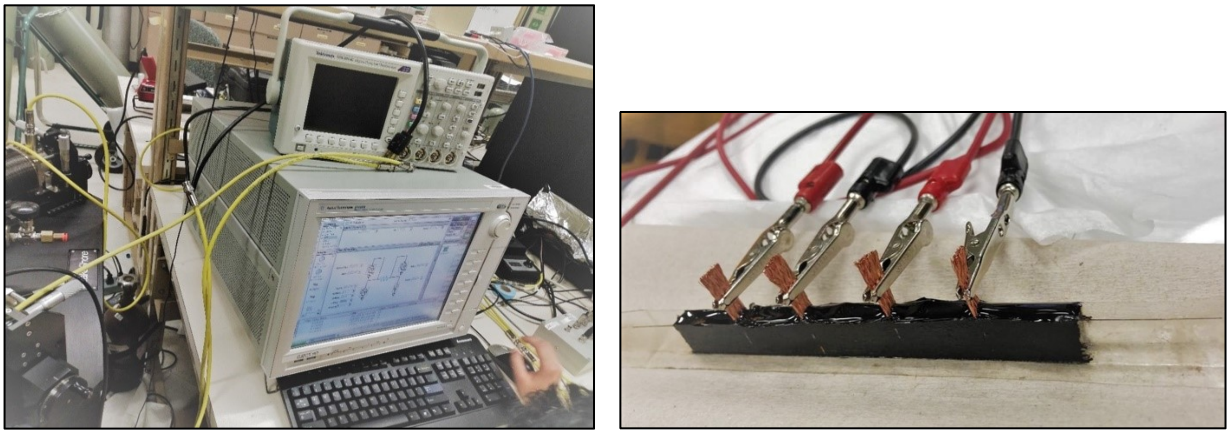

(a) (b)

Figure 3.7: Four-probe conductivity test: (a) semiconductor device analyzer, and (b) four-probe measurement setup.

During the test, two measurements were made for each sample. Figures 3.8 to 3.11 show the measured relationships among the electric current, voltage, and resistance.

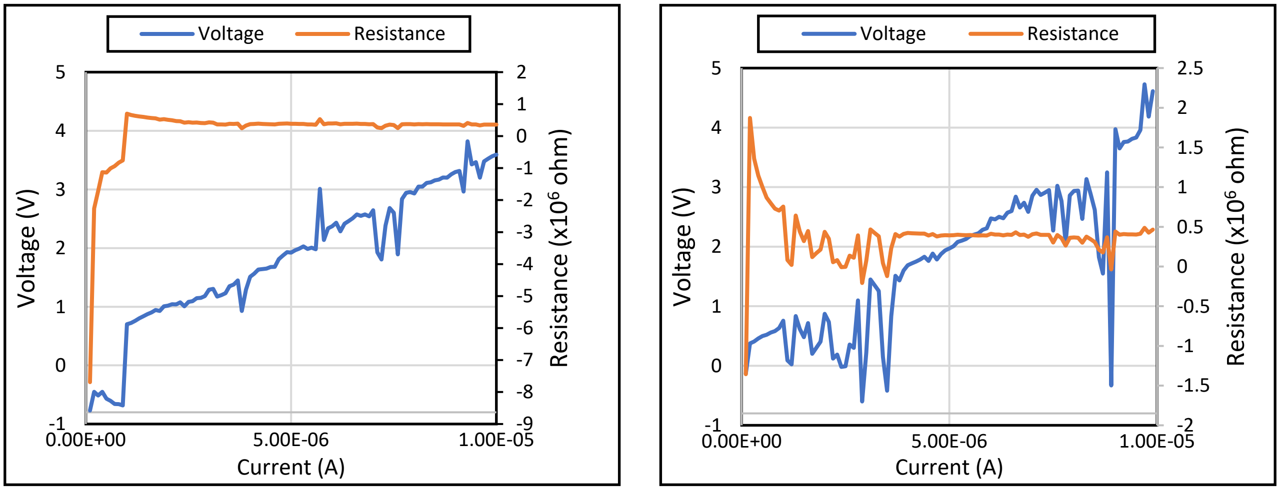

(a) (b)

Figure 3.8: Applied current vs. voltage and resistance for sample number 1 from: (a) test 1 (b) test 2.

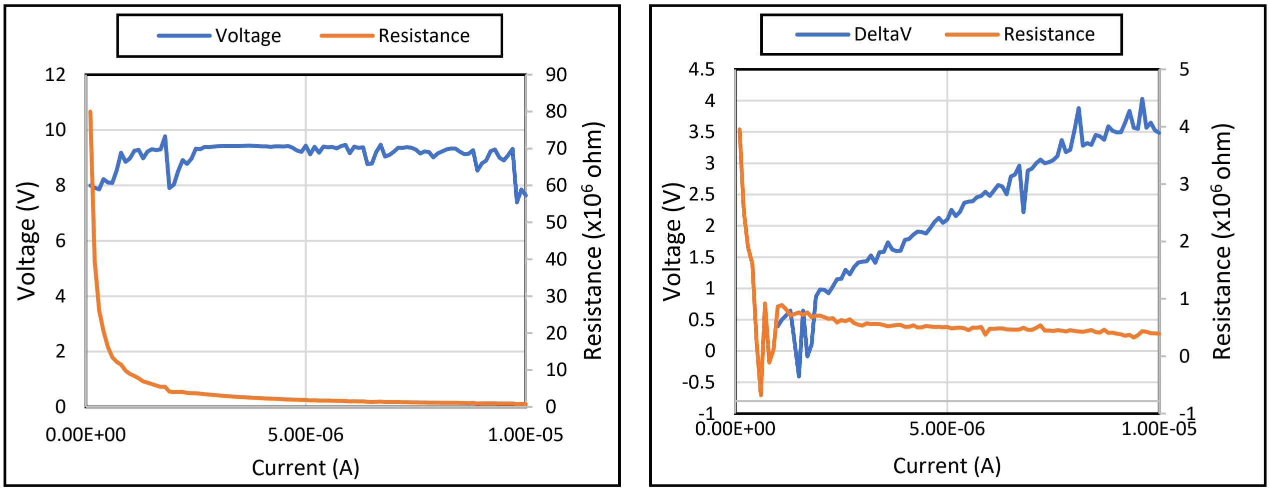

(a) (b)

Figure 3.9: Applied current vs. voltage and resistance for sample number 2 from: (a) test 1 (b) test 2.

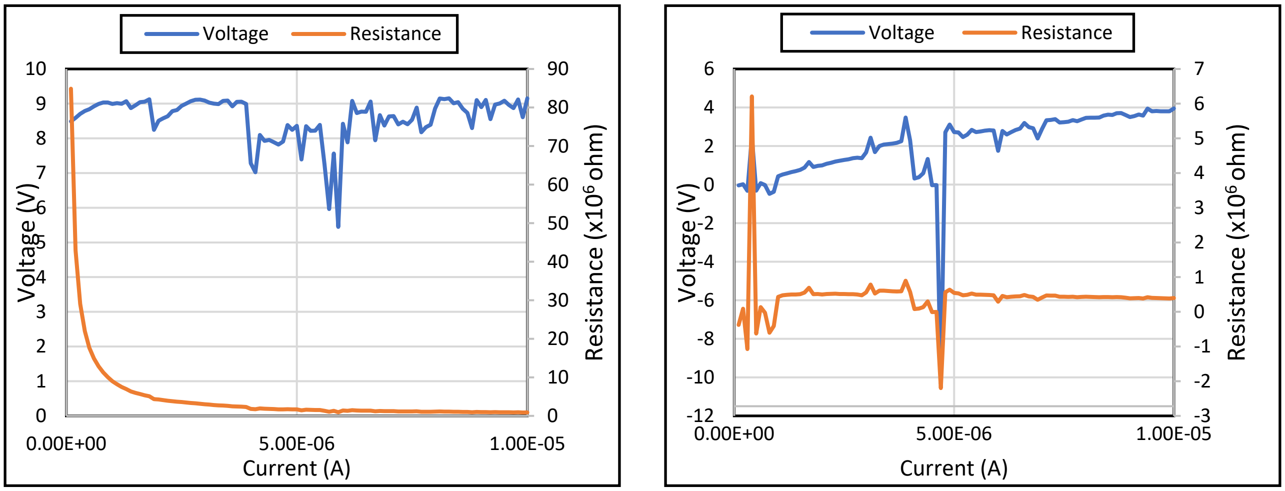

(a) (b)

Figure 3.10: Applied current vs. voltage and resistance for sample number 3 from: (a) test 1; (b) test 2.

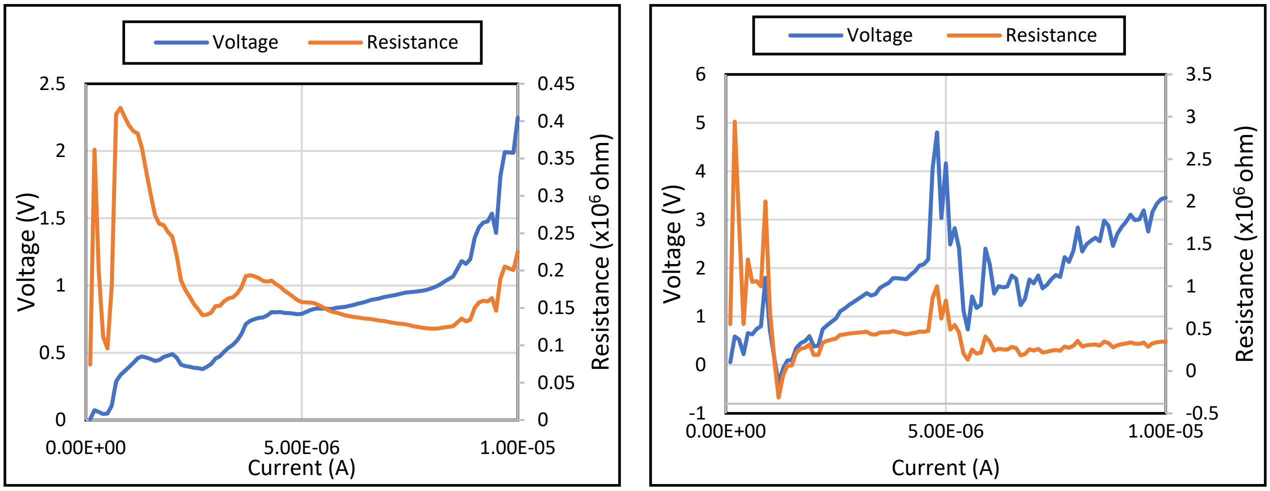

(a) (b)

Figure 3.11: Applied current vs. voltage and resistance for sample number 4 from: (a) test 1; (b) test 2.

Based on the measured resistance, the resistivity and conductivity are calculated using the following equations:

$$\rho = R\frac{A}{L} \tag{3.1}$$

(3.2)

where is the resistivity, σ is the conductivity, *R* is the electrical resistance of the sample, *L* is the distance between the measurements and *A* is the cross-sectional area of the sample. Table 3.6 summarizes the results, and Figures 3.12 to 3.14 show the plotted values.

Table 3.6: Average resistance, resistivity, and conductivity results.

Sample	Average Resistance (Ohm)	Resistivity (Ohm*m)	Conductivity (mS/m)
Control 3	3.67E+05	1.06E+03	9.45E-01
Control 4	3.42E+05	9.84E+02	1.02E+00
Taco 1	1.56E+06	4.48E+03	2.23E-01
Taco 2	4.67E+05	1.35E+03	7.43E-01
GNP 1	1.42E+06	4.08E+03	2.45E-01
GNP 2	3.96E+05	1.14E+03	8.76E-01
GNP+Taco 1	1.53E+05	4.41E+02	2.27E+00
GNP+Taco 2	3.60E+05	1.04E+03	9.64E-01

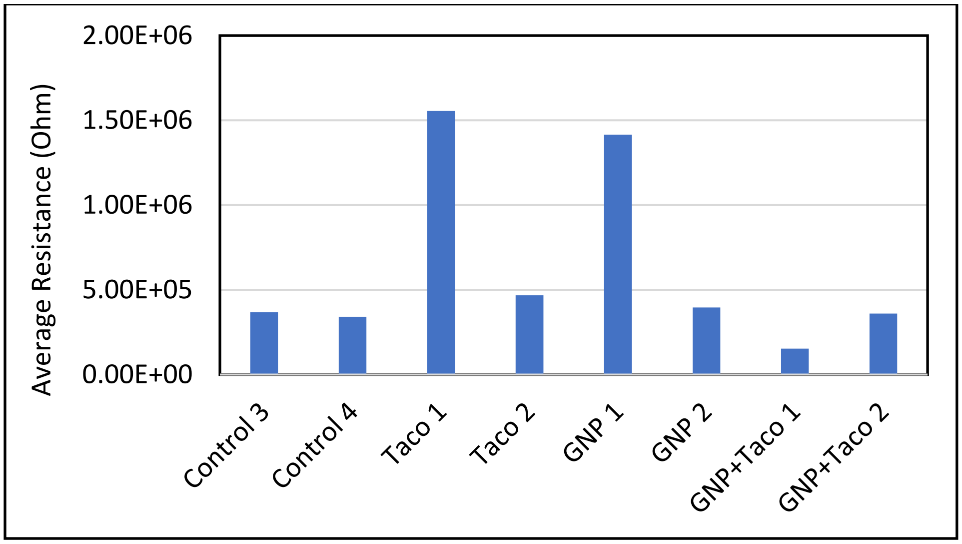

Figure 3.12: Average resistance of the eight measurements.

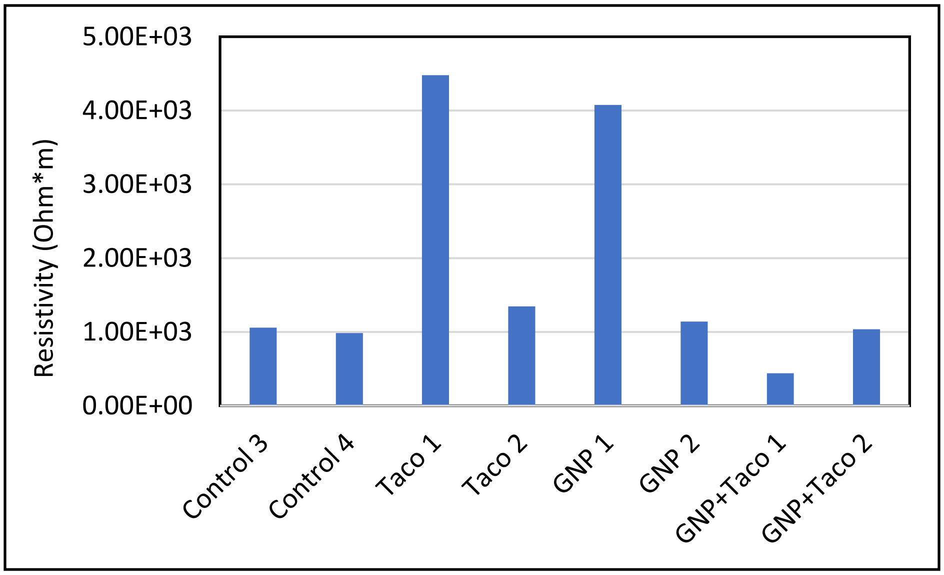

Figure 3.13: Resistivity of the eight measurements.

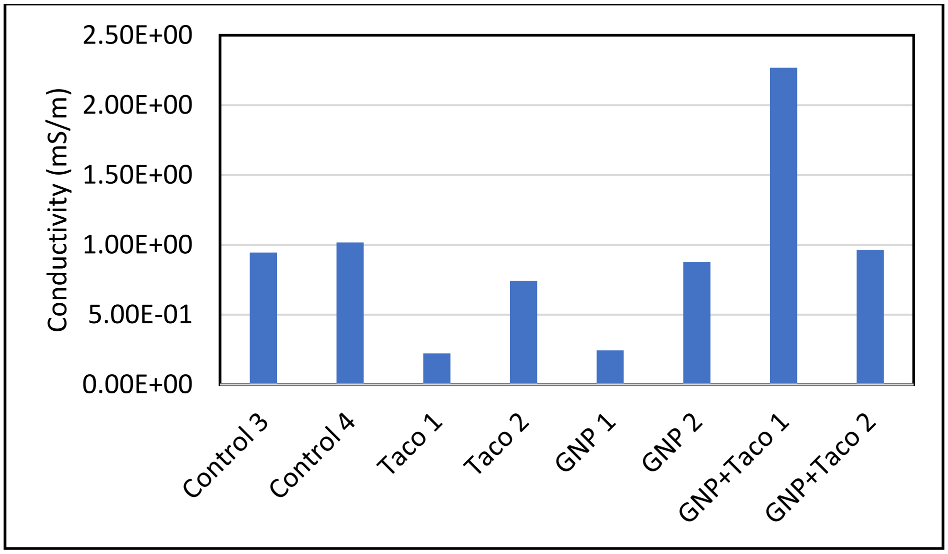

Figure 3.14: Conductivity of the eight measurements.

Compared to the control samples, the addition of GNP or taconite alone (6% by weight of the binder) does not lead to an improvement of electrical conductivity. The basic mechanism for enhancing the electrical conductivity through nano-particle addition is that the particles can be dispersed to the extent that the spacing between them is small enough for the electrons to hop. This mechanism can be analyzed by the percolation theory. An analytical model was recently proposed for the percolation threshold of nanocomposites containing 3D random distributed disc-shaped nano-particles based on the average interparticle distance approach:

$$V_{tr} = \frac{27\pi d^2 t}{4(d + s_{ip})^3}$$

where V_{tr} is the threshold of volume ratio of the binders, d is the diameter of the particle, t is the thickness of the particle, s_{ip} is the maximum spacing that allows for electron hopping to take place between adjacent conductive filler due to quantum-mechanical tunneling. The s_{ip} is expected to be in the order of 10 nm, which can be neglected compared to *d*.

For GNP used in this study, Equation 3.3 gives $V_{tr} \approx 21\%$ ($d/t = 100$). However, it should be pointed out that Equation 3.3 was derived based on the assumption that the nano-particles are uniformly distributed in space and size, which was unlikely to be achieved in GNP-reinforced asphalt binders. Therefore, the actual percolation threshold could be much higher than the prediction by Equation 3.3. On the other hand, after increasing the GNP to 10% by weight of the binder, the mix could not be poured into the mold at a temperature lower than 180°C. Raising the temperature above 160°C may affect the binder properties and for this reason, the percent of GNP in the binder by weight was limited to 6%. This practical difficulty of mixing limits the maximum amount of GNPs that can be added to the binders.

The foregoing analysis shows that adding 6% GNP alone may not lead to a considerable improvement of the electrical conductivity. In fact, the present test shows that the addition of 6% GNP or 6% taconite leads to a decrease in conductivity. However, when a combination of GNP and taconite is added, the conductivity is improved. One possible reason could be that the addition of taconite on top of GNP may provide a medium that enhances the dispersion of GNPs, and thus creates a more effective electron hopping network. The observed improvement could also be due to the chemistry among GNP, taconite, and asphalt binder, which requires deeper investigation.

Based on the results of the present test, it may be concluded that the combination of 6% GNP and 6% taconite gives the most pronounced improvement of electrical conductivity. The GNP-taconite modified asphalt materials could potentially be used for damage sensing since the existence of material damage could lead to a considerable decrease in electrical conductivity. In the next chapter, a mathematical model for the relationship between the extent of material damage and the change of electrical conductivity will be developed.

CHAPTER 4: DERIVATION OF THE RELATIONSHIP BETWEEN THE DAMAGE EXTENT AND ELECTRICAL RESISTANCE

The research team investigated the relationship between the damage of the material and the relative change of its electrical resistance by 1) deriving a mathematical model based on the analogy between the electrostatic field and the elastostatic field under anti-plane shear loading, and 2) performing four-probe electrical conductivity experiments on GNP-taconite modifies binders with different notch depths.

4.1 MATHEMATICAL MODEL

To further exploit the GNP-taconite modified asphalt materials for damage sensing in engineering practice, it would be desirable to develop a mathematical model, through which damage extent can be directly related to the measured fractional change in electrical resistance. To determine the effect of material damage on the overall electric resistance of a conductive specimen, it should be noted that the solution to the 2D electrostatic field is mathematically analogous with the solution to the 2D elastostatic field under anti-plane shear loading (Khripin *et. al.*, 2005; McMeeking, 1990; Suo, 1993). This analogy will be reviewed then the known elastostatic solution will be borrowed to derive the relationship between the electrical resistance and damage extent.

Consider a 2D specimen subjected to the electrostatic field shown in Figure 4.1(a). The equation of continuity for the electrostatic field states:

$$\partial J_x / \partial x + \partial J_y / \partial y = -\partial \rho / \partial t \tag{4.1}$$

where J_i ($i = x, y$) = components of current density in x- and y- directions, and ρ = electric charge density. The current density is related to the electric field E through Ohm's law, i.e. $E_i = \sigma^{-1} J_i$ ($i = x, y$), σ = conductivity and the electric field can further be derived from the electric potential φ: $E_x = -\partial\varphi/\partial x$, $E_y = -\partial\varphi/\partial y$.

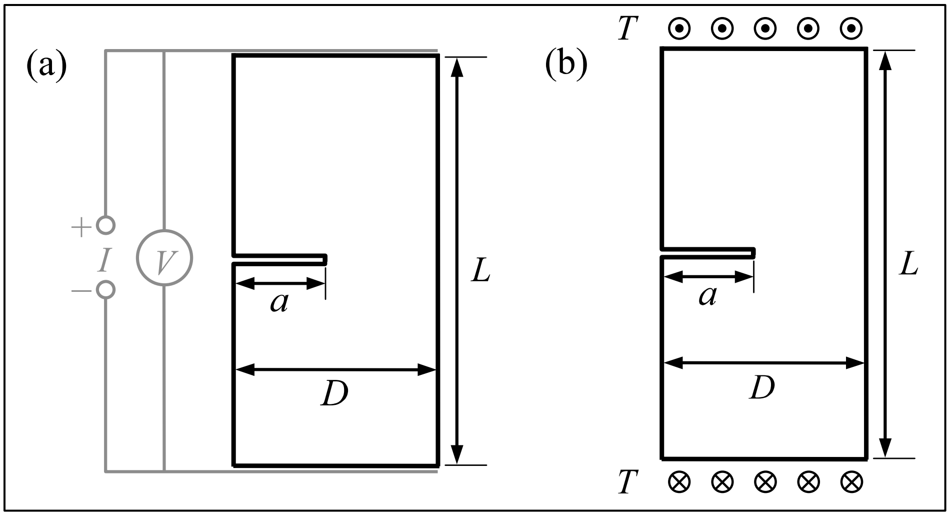

Figure 4.1: A damaged specimen with notch length a: (a) crack detection with conductive plates attached to the ends of the specimen; (b) mathematical analogy of anti-plane shear applied to the ends of the specimen.

Meanwhile, for an elastostatic field under anti-plane shear loading, the equilibrium equation can be written as:

$$\partial \tau_{zx} / \partial x + \partial \tau_{zy} / \partial y = -f \tag{4.2}$$

where τ_{zi} ($i = x, y$) = shear stresses, and f = body force. Hooke's law states $\tau_{zi} = G\gamma_{zi}$ (G = shear modulus, γ_{zi} = shear strain). Based on the small deformation theory, the shear strain can be calculated from the out-of-plane displacement u_z: $\gamma_{zx} = \partial u_z / \partial x$, $\gamma_{zy} = \partial u_z / \partial y$. By comparing the governing equations for electric and elastostatic fields, it is evident that the current density is analogous to the shear stress, the electric field is analogous to the shear strain, and the electric potential is analogous to the out-of-plane displacement.

The electrical resistance can be computed from $R = V/I$, where V = voltage change (i.e. change of electric potential φ) across the specimen and I = prescribed electric current running through the specimen. Based on the abovementioned mathematical analogy, it is evident that the overall electric resistance of the specimen is analogous to the elastic compliance of the specimen C_τ under anti-plane shear loading, i.e.:

$$R = \frac{V}{I} \sim \frac{\Delta u_z}{T} = C_\tau \tag{4.3}$$

where Δu_z = relative out-of-plane displacements at locations where the electric resistance is measured, and T = total anti-plane shear force applied at these locations (Figure 4.1b).

It is expected that both electrical resistance and material compliance would possibly vary with the damage extent. Based on Equation 4.3, it is clear that the effect of damage extent on the electrical resistance is the same as that on the elastic compliance under anti-plane shear loading, i.e.:

$$R(w)/R_0 = C_\tau(w)/C_0 = f(w) \tag{4.4}$$

where w = damage parameter commonly used within the framework of continuum damage mechanics, (w ranges from 0 (intact material) to 1 (complete damage)), R_0, C_0 = electrical resistance and elastic compliance under anti-plane shear loading of an intact specimen (i.e. $w = 0$), respectively. Equation 4.4 indicates that elastic stress analysis can be used to calculate the dependence of anti-plane shear compliance of the specimen on the damage extent $C_\tau(w)$, which is equivalent to the dependence of the electrical resistance on the damage extent.

The focus of this study is limited to the case where the damage is represented by a discrete macro-crack. This is commonly encountered in many structures made of cementitious materials due to damage localization mechanism (Bažant & Planas, 1998). It is clear that, for a given electric resistance measurement, anti-plane shear loading must be applied in the elastostatic analogy at the locations where the voltage is measured.

Based on the linear elastic fracture mechanics, the energy release rate at the crack tip $\mathcal{G}$ can be calculated either from the stress intensity factor or from the complementary potential energy, i.e.

$$\mathcal{G} = K^2/2G = \left.\frac{\partial U^*}{b\partial a}\right|_T \tag{4.5}$$

where K = stress intensity factor, a = crack length, b = specimen width in the transverse direction, U^* = complimentary potential energy, and T = applied anti-plane shear force. Within the framework of linear elasticity, $U^* = 0.5C_\tau T^2$ is valid. Therefore, Equation 4.5 leads to:

$$\frac{\partial C_\tau}{\partial a} = \frac{bK^2}{GT^2} \tag{4.6}$$

The stress intensity factor K can always be written as $K = Tb^{-1}D^{-1/2}\,k(\alpha)$, where D = specimen dimension, $\alpha = a/D$ = relative crack length, and $k(\alpha)$ = dimensionless stress intensity factor, which is often known for many specimen geometries under anti-plane loading (Bažant & Planas, 1998). D can be defined as the specimen width in the direction of the crack, then α can directly be used as the damage parameter used in Equation 4.4 since $\alpha = 0$ represents an intact state and $\alpha = 1$ represents the complete damage state. By integrating Equation 4.6, the anti-plane shear compliance for a given relative crack length α is obtained:

$$C_{\tau}(\alpha) = C_{\tau 0} + \int_0^{\alpha} \frac{k^2(\alpha')\mathrm{d}\alpha'}{bG} \tag{4.7}$$

With Equation 4.4, the effect of crack length on the overall electric resistance of the specimen is obtained:

$$\frac{R(\alpha)}{R_0} = 1 + \frac{\int_0^{\alpha} k^2(\alpha')\mathrm{d}\alpha'}{bGC_{\tau 0}} \tag{4.8}$$

The specimen shown in Figure 4.1b can be taken as an example. The dimensionless stress intensity factor of this geometry can be derived from the mode III stress intensity factor (Bažant & Planas, 1998):

$$k(\alpha) = \sqrt{2\tan\frac{\pi\alpha}{2}} \tag{4.9}$$

The compliance C_0 of an intact specimen without damage that is subjected to anti-plane shear loading can be easily shown to be: $C_{\tau 0} = L/GbD$. Therefore, a closed-form expression for a size-independent parameter β_R for the fractional change in resistance as a function of the relative crack length for a specimen with an infinitesimally small crack width can be derived:

$$\beta_R = r_a \frac{\Delta R(\alpha)}{R_0} = r_a\left(\frac{R(\alpha)}{R_0} - 1\right) = -\frac{4}{\pi}\ln\left|\cos\left(\frac{\pi\alpha}{2}\right)\right| \tag{4.10}$$

where $r_a = L/D$ is the aspect ratio of the specimen.

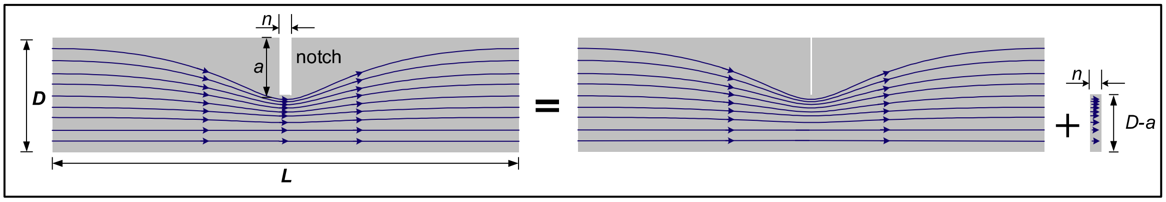

Figure 4.2: Streamlines flowing through a specimen with a finite notch width.

In the case of a small but finite crack width n, the narrow strip of reduced cross-sectional area at the crack plane will increase the electrical resistance as compared to the case with an infinitesimally small crack width. Due to symmetry, the streamlines passing through the crack plane are parallel to the direction of current flow which allows us to treat the electrical resistance of the specimen with finite crack width as series coupling of electrical resistance through a specimen with infinitesimally small crack width, a narrow strip of width n, and a reduced cross-section area $bD(1-\alpha)$, as shown in Figure 4.2. This simple correction remains valid so long as the crack width is not too large that the elastostatic field is severely affected:

$$\beta_R = r_a \frac{\Delta R(\alpha)}{R_0} = -\frac{4}{\pi} \ln\left|\cos\left(\frac{\pi\alpha}{2}\right)\right| + \frac{n}{D}\left(\frac{\alpha}{1-\alpha}\right) \tag{4.11}$$

4.2 EXPERIMENTAL INVESTIGATION

For the experimental investigation, specimens were prepared from two mixes. The control mix uses binder PG 58-28, whereas the other mix uses binder PG 58-28 modified by 6% taconite concentrate and 6% GNP 4827. For each mix, notched specimens of different notch depths were prepared. The notch depth represents the existing damage extent. Table 4.1 shows the information of the test specimens.

Table 4.1: Mix designs and notch sizes used in the GNP-concentrate notched samples.

Sample No.	Notch size	Type
1	No notch	PG 58-28
2	20%	PG 58-28
3	40%	PG 58-28
4	No notch	PG 58-28 + 6% taconite concentrate + 6% GNP 4827
5	20%	PG 58-28 + 6% taconite concentrate + 6% GNP 4827
6	40%	PG 58-28 + 6% taconite concentrate + 6% GNP 4827

The GNP taconite modified binder was prepared in two steps: 1) mix GNP 4827 and heated binder (PG 58-28) in a high-velocity shear mixing device for one hour, and 2) add taconite concentrate into the GNP modified binder and hand-stirred for about 5 minutes (the taconite concentrate was not mixed in the shear mixing device due to the size of the concentrate particles).

Similar to Chapter 3, the electrical conductivity was measured by using a four-probe method. The mix was poured into the beam molds with four cooper electrodes, as shown in Figure 4.3.

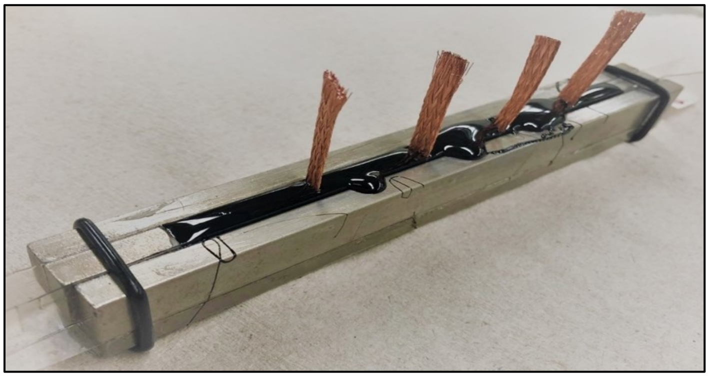

Figure 4.3: Sample preparation: beam molds with four copper electrodes.

All the beams were placed in the refrigerator for 24 hours. A blade was used to cut the notches that were held in place by a small foil film, as shown in Figure 4.4. The foil film was used to prevent contact of the binder, ensuring the notch size.

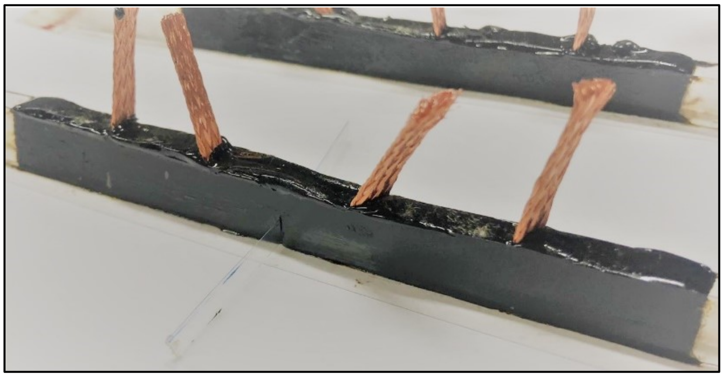

Figure 4.4: Sample preparation: foil film holding the notch.

After the notch was cut, the beams were put back to the refrigerator for 21 days before the experiment was performed. The electrical conductivity tests were performed on the samples using the same method as described in Chapter 3: the outer two probes were used to supply electrical current to the specimens, while the inner probes were used to measure the voltage. Figure 4.5 shows the probes used in the test.

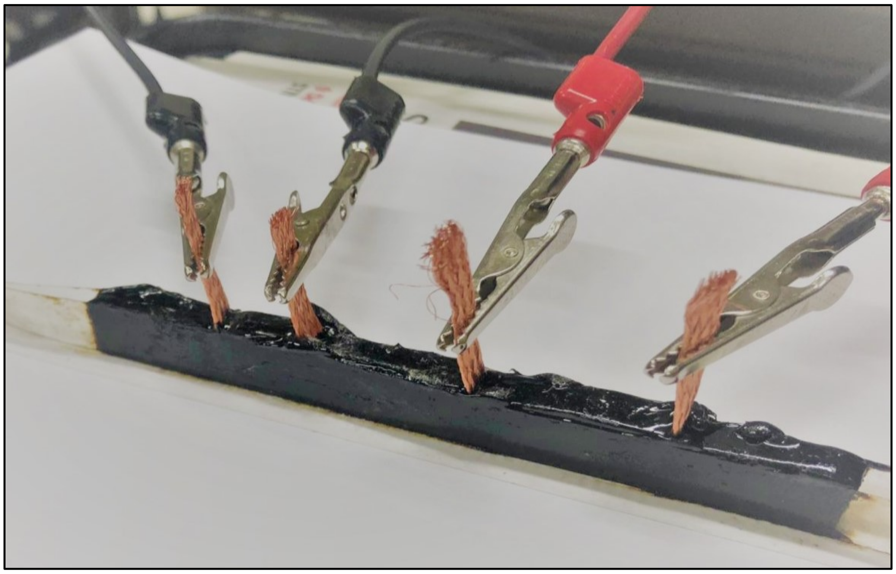

Figure 4.5: Four-probe measurement setup.

The semiconductor device analyzer *Agilent Technologies B1500A* applied the current sweep, which increased in steps from 0.0001 to 0.1A, and the corresponding voltage was measured at each step. The measured voltage and resulting resistance values were plotted in Figures 4.6 to 4.8.

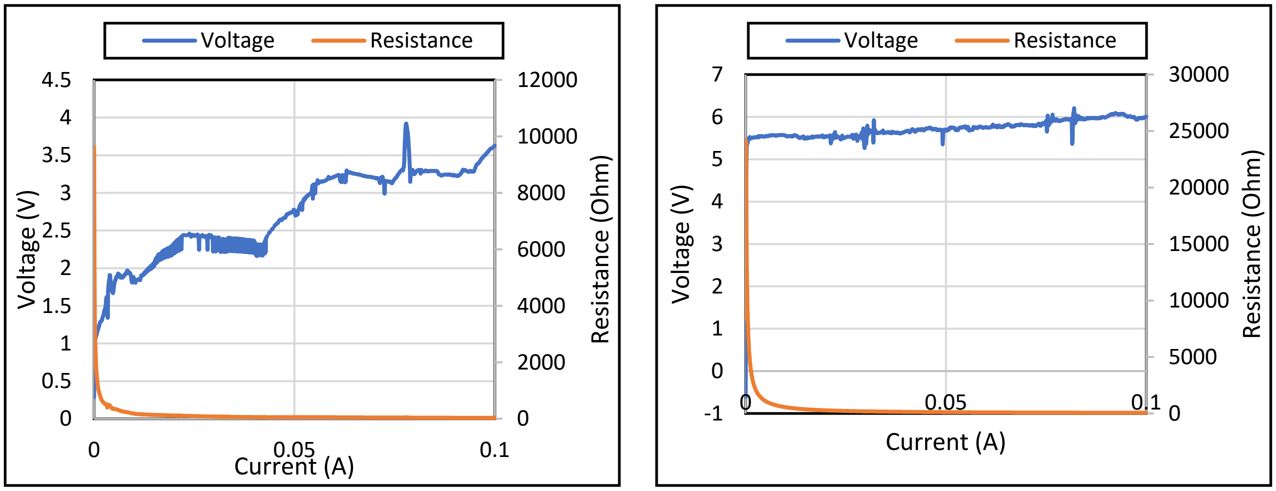

(a)

(b)

Figure 4.6: Applied current vs. voltage and resistance for: (a) sample 1 and (b) sample 2

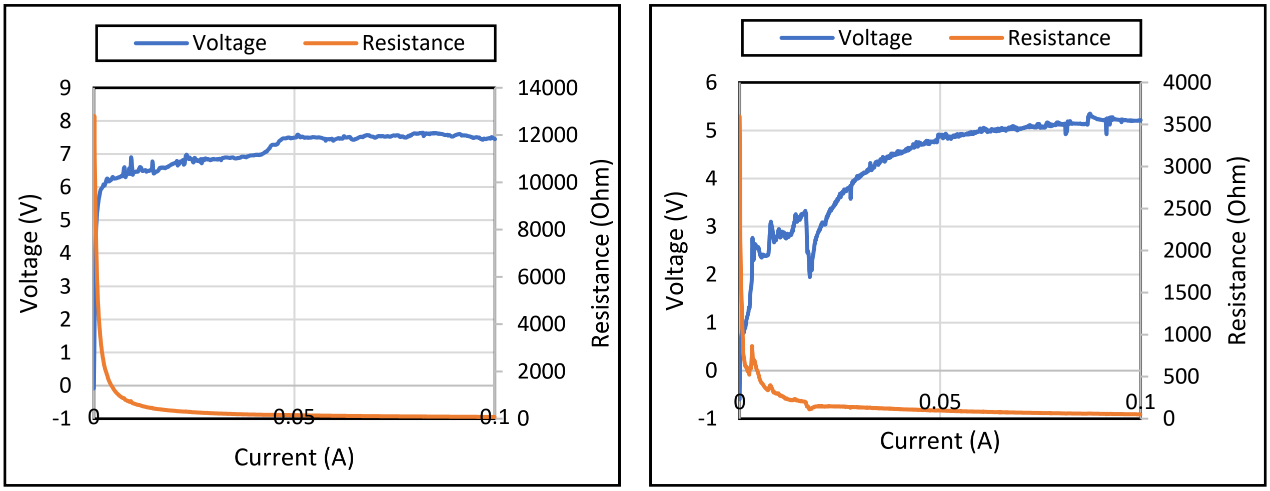

(a)

(b)

Figure 4.7: Applied current vs. voltage and resistance for: (a) sample 3 and (b) sample 4

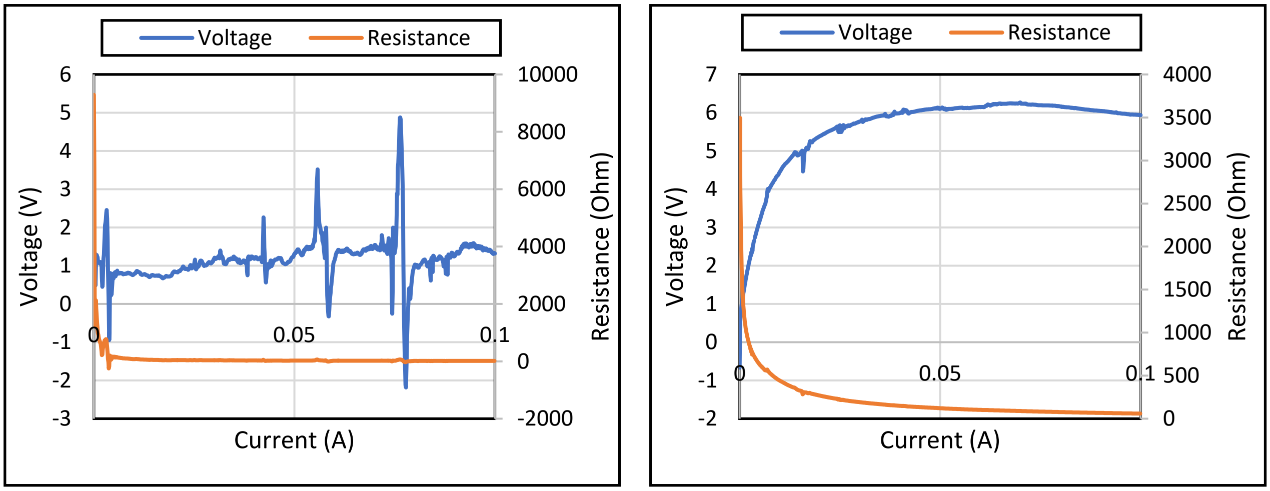

(a) (b)

Figure 4.8: Applied current vs. voltage and resistance for: (a) sample 5 and (b) sample 6

Table 4.2 shows the resistance, the calculated conductivity, and conductivity, which were obtained using equations 4.1 and 4.2.

$$\rho = R\frac{A}{L} \tag{4.1}$$

(4.2)

where is the resistivity, σ is the conductivity, *R* is the electrical resistance of the sample, *L* is the distance between the measurements and *A* is the cross-sectional area of the sample. Figures 4.9 to 4.11 show the plotted values.

Table 4.2: Average resistance, resistivity, and conductivity results.

Sample	Average Resistance (Ohm)	Resistivity (Ohm*m)	Conductivity (S/m)
Control	126	0.363	2.755
Control 20% notch	364.7	0.84	1.19
Control 40% notch	386	0.667	1.499
GNP+Taco	152.3	0.439	2.28
GNP+Taco 20% notch	75.9	0.175	5.718
GNP+Taco 40% notch	209.9	0.363	2.757

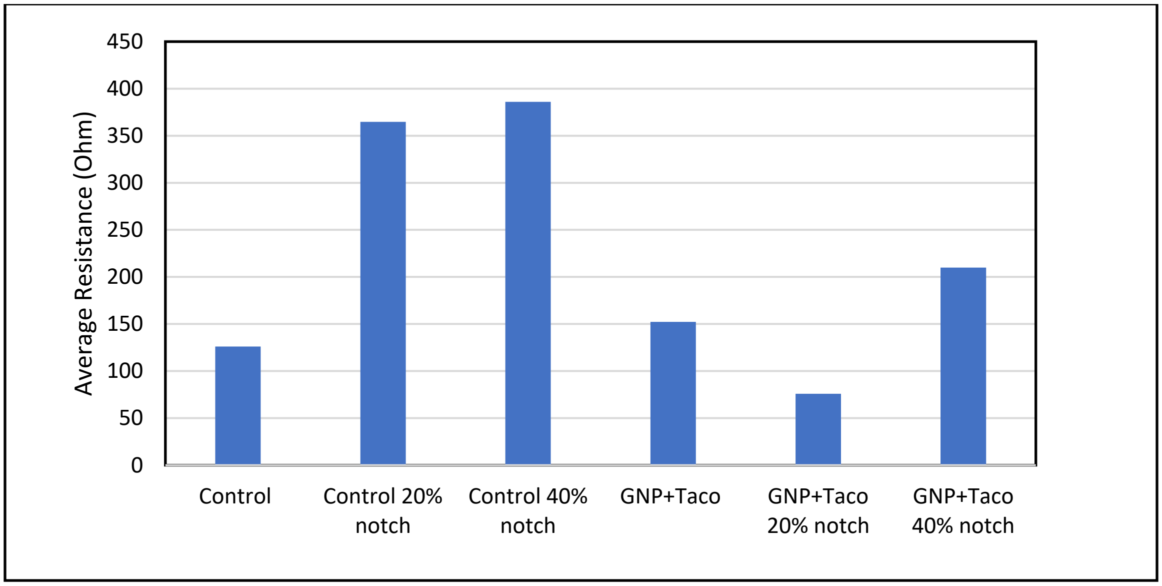

Figure 4.9: Average resistance of the six measurements

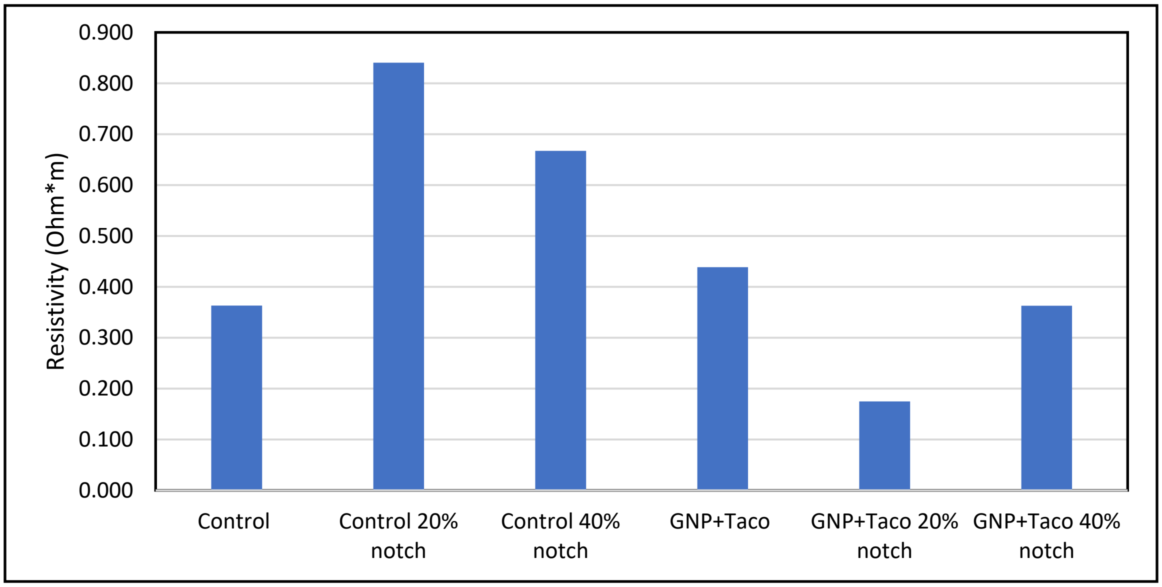

Figure 4.10: Resistivity of the six measurements

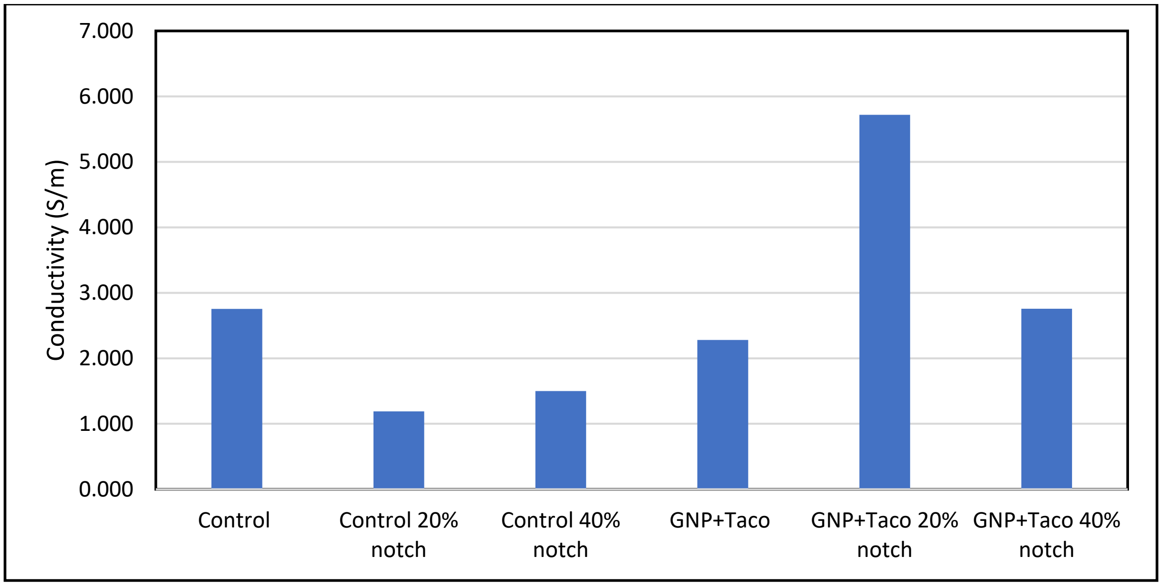

Figure 4.11: Conductivity of the six measurements

4.3 DISCUSSION

Compared to the tests performed in Chapter 3, the most recent results show much lower resistance and therefore, much higher conductivity. After comparing both procedures, the research group determined that such discrepancy is due to the presence of moisture in the most recent batch of specimens. The tests in Chapter 3 were performed in January, when the air is very dry, whereas the tests in this chapter were performed in June when air humidity was very high. The cold binder in contact with warm moist air caused the formation of water droplets on the surface that, even after drying before the measurements, are believed to have influenced the test results.

The humid environment worked as a new boundary condition. Specimens subjected to moisture within the sample or in the air can generate overestimated test results (Li *et. al.*, 2016). The very high dielectric constant of liquid water, usually attributed to its large liquid phase dipole moment, is shown in Table 4.3:

Table 4.3: Dielectric values air, water, ice, and different subgrade soils and road materials (Saarenketo, 2006)

Material	Dielectric value
Air	1
Water (fresh)	81
Ice	4
Bedrock (granite)	5–7
Peat (natural)	60
Peat (under road)	40
Clay	25–40
Silt	16–30
Silty sand	Silty sand 7–10
Sand	Sand 4–6
Gravel	Gravel 4–7
Glacial till (moraine)	8–18
Asphalt / other bituminous pavements	4–8 (if slag present 8–
Concrete	8–10
Gravel road wearing course	12–14
Crushed base	6–8
Bitumen bound base	6–7
Cement bound base	8–10
Insulation boards (new)	2–2.5
Road structures in average (new/dry)	5
Road structures in average (normal)	6
Road structures in average (wet/old)	7–8
Gravel road structures in average	7–9
Frozen road structures (normal)	5
Frozen road structures (wet/old)	6

Therefore, the different results are due to the difference in the measurement conditions.

CHAPTER 5: INVESTIGATION OF SELF-HEALING CAPACITY OF GNP-TACONITE MODIFIED ASPHALT MIXTURES

In this task, the research team performed laboratory experiments to investigate the damage healing capacity of GNP-taconite modified asphalt mixtures. Asphalt mixture specimens were preloaded to induce a certain level of damage. Different methods were used to evaluate if damage is reversed when microwave energy is applied to the asphalt specimens, and healing occurs.

5.1 INITIAL EXPERIMENTAL WORK

In the initial experimental work, asphalt mixture beams were first prepared and partially damaged using multiple loading cycles in three-point bending, followed by exposure to microwave energy, and then evaluated to determine if healing occurred. Based on the results of a literature search, we evaluated if healing occurred in asphalt mixtures prepared with Graphite nano-platelet (GNP) and Taconite Concentrate (CONC) by performing additional cycles of reloading of the microwaved asphalt mixture beams and comparing the magnitude of crack mouth opening before and after microwaving.

5.1.1 Materials and Test Specimen Preparation

To prepare the asphalt mixture specimens, loose mix from cell 22 at MnRoad, prepared with a PG58H-34 binder, was used. The control mixture, labeled “mix 1”, represents the original loose mix with no additives. Mix 2 contains loose mix plus 2% taconite concentrate by weight of the mix. Mix 3 contains loose mix plus 2% taconite concentrate by weight of the mix plus 3% GNP by weight of the binder. Mix number 4 contains loose mix plus 3% GNP by weight of the binder.

A Superpave gyratory compactor was used to prepare one cylinder for each mixture. All four cylinders were compacted to 100 gyrations and were stored at room temperature for three days. Eight beams were then cut from each cylinder, as follows: 6 inch long, by 1.5 inch tall, by .75 inch wide. A small notch was placed at the bottom of the beam to induce cracking upon loading.

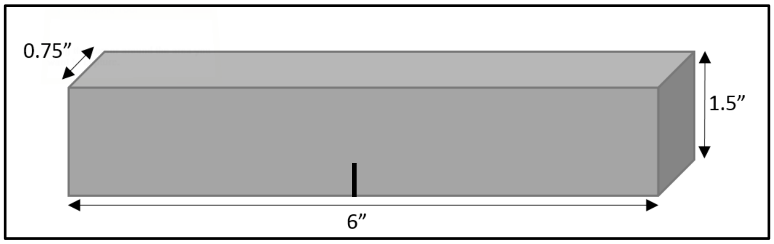

Figure 5.1: Asphalt mixture specimen.

5.1.2 Preloading Procedure to Induce Partial Damage

All testing was performed at -24°C, based on the low-temperature limit of the binder grade 58H-34. First, three-point bending tests were performed for each of the 4 mixtures to determine their strength, and therefore the peak load. For each mixture, three replicate tests were performed, and the results are shown in Table 5.1.

Table: 5.1: Results from the Strength Tests to Failure.

Beam ID	Force, KN	B, mm	Notch depth, mm	Stress, MPa
Mix 1: Control				
2017-BCG-STR-1X-6_-24	-0.74	20	33	-6.12
2017-BCG-STR-1X-7_-24	-0.74	20	33	-6.10
2017-BCG-STR-1X-8_-24	-0.68	20	33.5	-5.41
Average	**-0.72**			
Mix 2: + Concentrate				
2017-BCG-STR-2C-8_-24	-0.78	20	33	-6.47
2017-BCG-STR-2C-6_-24	-1.00	20	33	-8.24
2017-BCG-STR-2C-7_-24	-0.76	19.5	33	-6.40
Average	**-0.85**			
Mix 3: +GNP+ Concentrate				
2017-BCG-STR-3GC-7_-24	-0.93	20	32	-8.16
2017-BCG-STR-3GC-4_-24	-0.98	20	32	-8.64
2017-BCG-STR-3GC-6_-24	-1.03	20	32	-9.08
Average	**-0.98**			
Mix 4: +GNP				
2017-BCG-STR-4G-7_-24	-0.96	20	33	-7.94
2017-BCG-STR-4G-6_-24	-1.07	20	35	-7.84
2017-BCG-STR-4G-8_-24	-0.74	20	32	-6.54
Average	**-0.92**			

Once the peak force was determined, a value equal to 70% of the peak load value was selected to run the fatigue tests required to induce partial damage in the test specimens. Each mixture beam received 2000, 3000, and 4000 cycles at 70% of the peak load. A crack mouth opening displacement (CMOD) gauge was placed at the notch of each beam to measure the crack mouth opening during loading. All loading cycles had a sine waveform. An example is shown in, as shown in Figure 5.2.

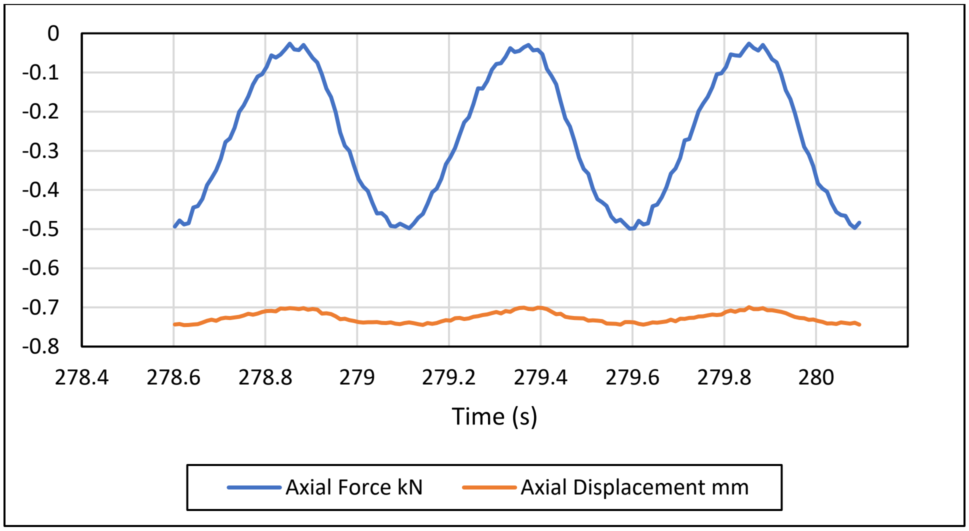

Figure 5.2: Axial displacement vs time.

For each loading cycle, the difference between the maximum and minimum values of the CMOD was recorded and reported as CMOD amplitude. An example is shown in Figure 5.3. Testing started with 2000 loading cycles of the beams. However, very small changes in CMOD amplitude were observed between cycle number 100 and the last cycle. The number was increased to 3000 cycles, and then to 4000 cycles for the last replicates tested.

For the control mix, three specimens were tested. For the three specimens tested, two of them were tested to 3000 cycles and one was tested to 2000 cycles. For Mix 2, with taconite concentrate, four specimens were tested; one was tested for 4000 cycles, two for 3000 cycles, and one for 2000 cycles. For Mix 3, containing both GNP and taconite concentrate, three specimens were tested; one was tested for 2000, one for 3000, and one for 4000 cycles, respectively. For Mix 4, containing only GNP, only two specimens were fully tested, both for 3000 cycles.

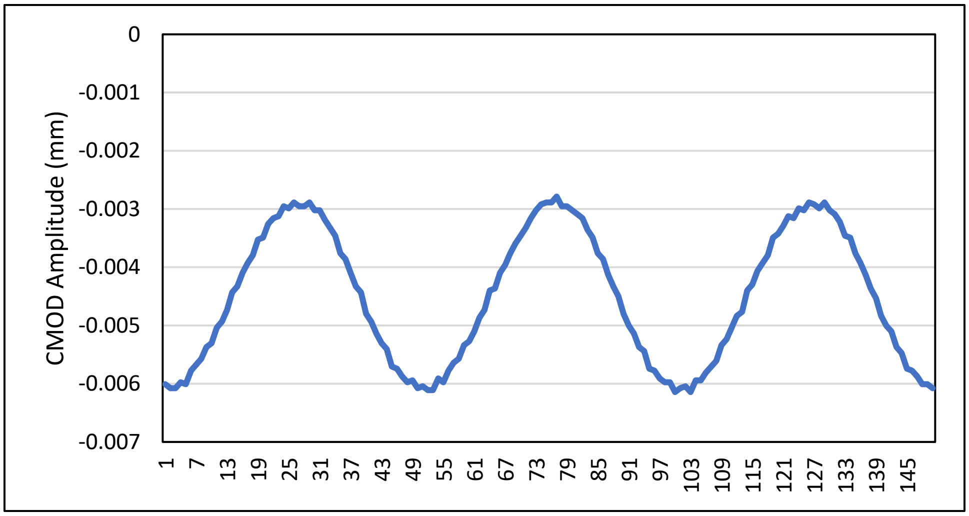

Figure 5.3: A sine waveform was used in testing the specimens.

5.1.3 Healing Procedure Using Microwave Energy

The idea of this preliminary healing experiment was to microwave the asphalt mixture beams until a temperature of 100°C was obtained. The first experiments were done on scrap pieces of the four different mixtures obtained in the process of cutting the rectangular beams from the compacted cylindrical specimens. The scraps were similar to the test specimens, except that they had some rounded edges. After several trials, it was found that the beams that contained taconite concentrate were 20 degrees warmer than the beams without taconite concentrate. It was also found that, to void overheating, it was best to microwave the beams in 30 seconds intervals and measure the temperature after each of them.

To heal the specimens after the initial fatigue loading, the beams for each type mix type were placed in the microwave together. The main purpose was to have consistent results, knowing that each different type of mix was heated at a different rate. The beams were microwaved for 30 seconds and the temperature was immediately checked, and the cycle was repeated until a temperature of 100°C was reached. After the beams reached the desired temperature, they were removed from the microwave and cooled with a fan. The beams were taken out of the microwave on the heating plate and were not individually moved until they reached room temperature. The beams rested until the following day when they were loaded again for 500 cycles.

5.1.4 Evaluation of Damage and Healing Using CMOD Results

We plot the CMOD amplitude of heated beams to evaluate the healing capability, as shown in Figures 5.4a to 5.4d. The results showed that there is a very small decrease in CMOD amplitude, which would suggest a sign of healing. However, the small change in CMOD amplitude does not provide clear evidence of healing capability. Figures 5.4a-5.4d showed that during the initial fatigue loading the COMD amplitude does not change significantly over time. This result indicates that the beam does not experience sufficient macroscopic damage even before the heating process. Therefore, to better evaluate the healing capability, we will need to either increase the loading amplitude or increase the number of loading cycles. Due to the randomness of material properties, increasing the maximum load to a higher level (90-95% of peak load) could result in monotonic failure of the specimen. Increasing the number of loading cycles would greatly prolong test duration. Therefore, we may conclude that using fatigue tests for evaluation of healing capability of GNP or CONC modified asphalt mixtures is not the most effective method.

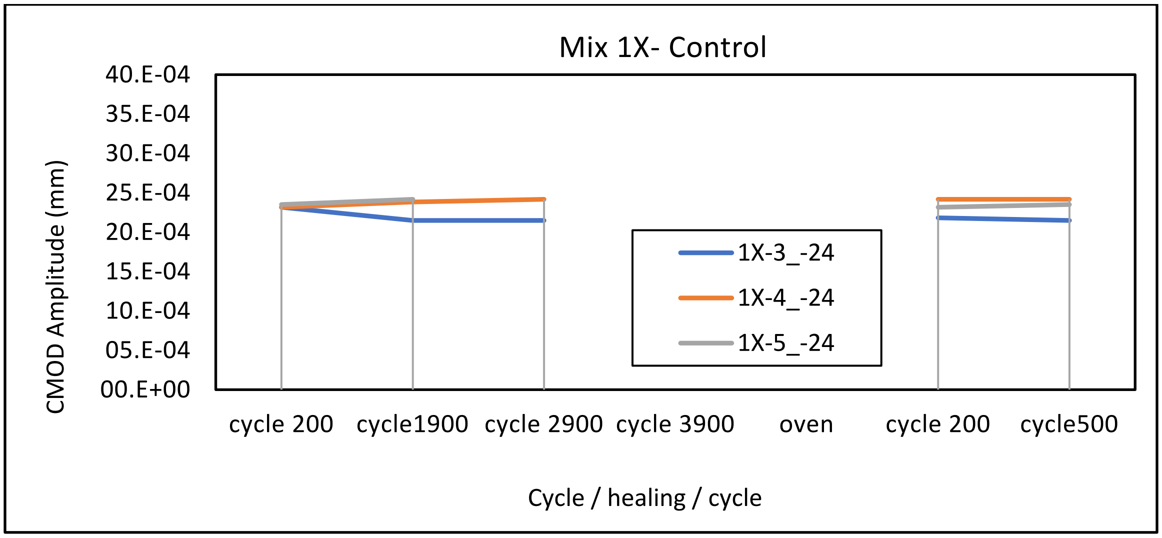

Figure 5.4a: Measured CMOD amplitude over cycles.

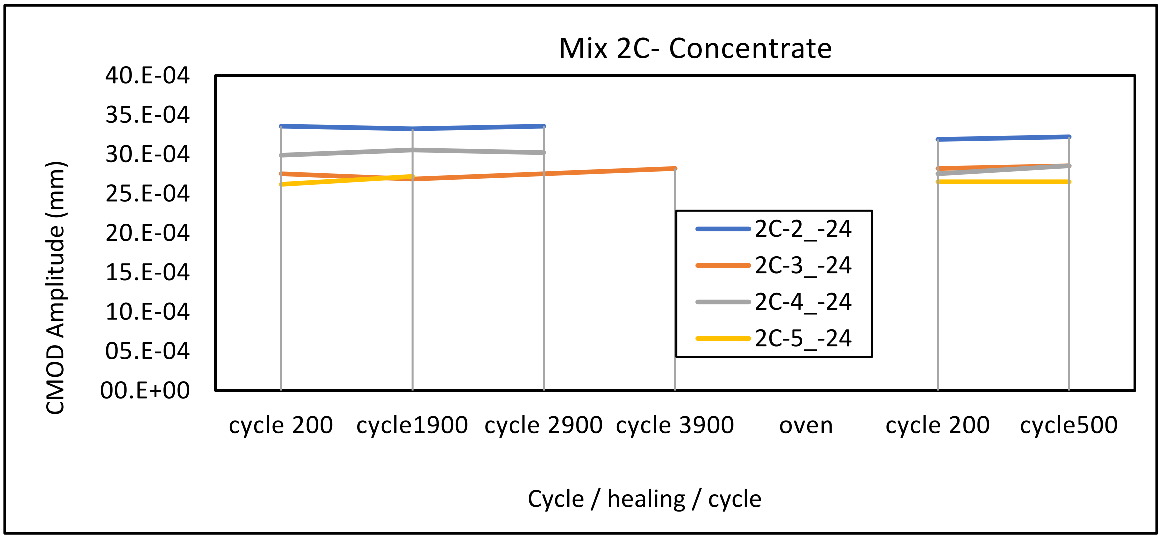

Figure 5.4b: Measured CMOD amplitude over cycles.

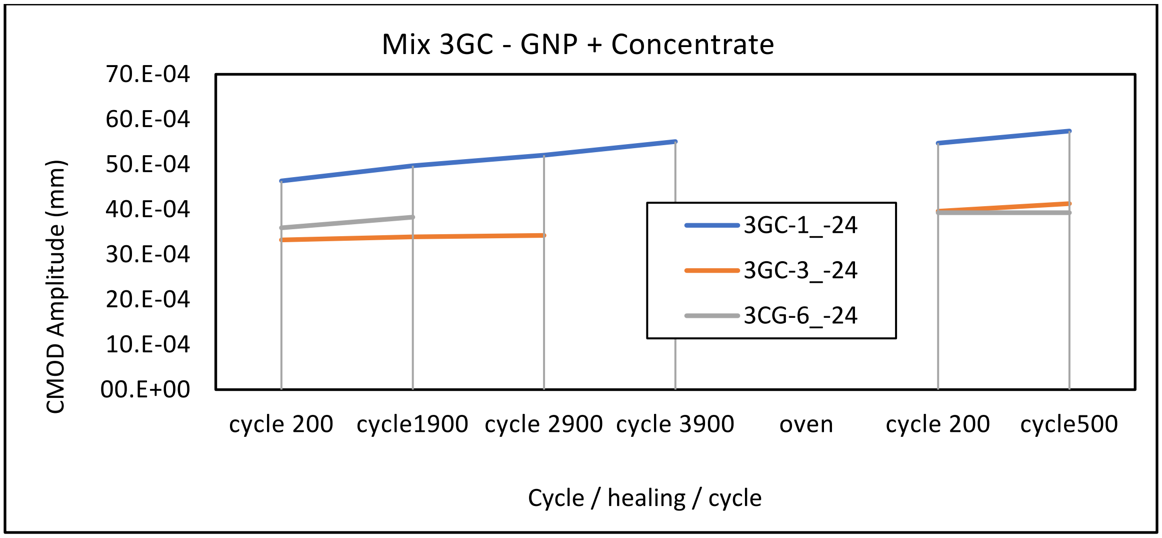

Figure 5.4c: Measured CMOD amplitude over cycles.

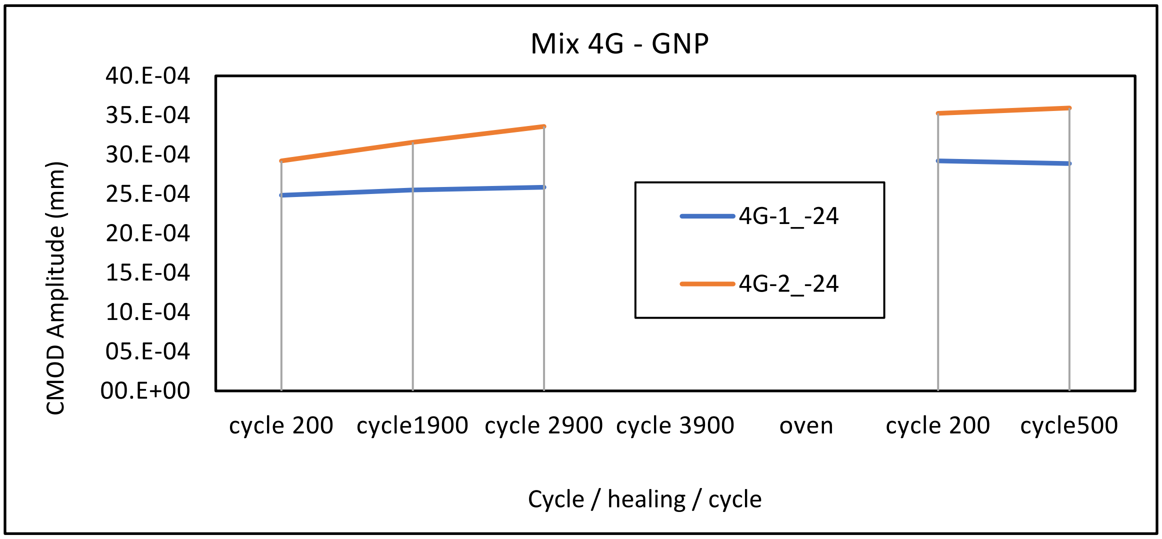

Figure 5.4d: Measured CMOD amplitude over cycles.

5.2 EXPERIMENTAL TESTING USING SCB

Based on the results obtained in the initial experimental work, it was decided to use only mechanical testing to evaluate damage and healing effects in asphalt mixtures. For this second round of testing, the semi-circular bend (SCB) test was used. The testing procedure, currently used to determine the fracture energy of asphalt mixtures at low temperatures, is detailed elsewhere (AASHTO, 2013). All SCB testing was done at -12°C.

One Superpave loose asphalt mixture was used to prepare all test specimens. Two types of specimens were prepared, as follows:

- Mixture 60-SPL was prepared with loose mix and 6% GNP (by weight, binder).

- Mixture 61-SPL was prepared with loose mix and 6% GNP (by weight, binder) and 1% concentrate (by weight of mixture).

For the first mixture, the GNP was added to the heated loose mix (at 135^{o}C) and mixed for 4 minutes. Two cylinders were made at 4% air void and then used to make 6 SCB samples. Each SCB sample is 31 mm thick, with a radius of 150 mm. A 15 mm notch was cut in the center, perpendicular to the base, with a 0.5 mm thick diamond blade.

For the second mixture, both the GNP and taconite concentrate were added to the heated loose mix (at 135^{o}C) and mixed for 4 minutes. One cylinder was used for all 6 samples. The following procedure was used in this experimental work.

- First test (for all samples):

- Testing was done following the AASHTO protocol using CMOD control. The test was stopped the load has decreased to 80% from the maximum (peak) load value. At 80% post-peak strength, the specimen is well expected to experience considerable damage. The test was performed at -12^{o}C. Before the testing, all the samples were conditioned at the testing temperature for two hours. The tested samples were stored in the fridge on a flat surface, at 6^{o}C.
- Based on the peak value, the samples (by type) were ordered in ascending order. The samples with the lowest, third, and fifth values were not treated in the microwave (labeled NON). The samples with the second, fourth and highest peak were treated in the microwave oven to heal (labeled Micro).
- The buttons were removed from all the samples after the SCB test.

- Microwave Treatment:

- The "Micro" samples were heated, seating on the semicircular side, one by one in the microwave oven for 1 minute and 30 seconds. The goal was to reach a surface temperature above the notch around 50°C. The initial plan, to cover the sample with aluminum foil (except for the notch area), did not work due to sparkling in the oven.
- At the end of the treatment, each sample was seated on a flat surface, on the same side, at room temperature for one hour, and then returned to the fridge at 6^{o}C. The measured temperature (with a non-contact thermometer), after the test, oscillated between 55°C and 70°C, depending on the target point (aggregate or mastic).

-Second test (for all samples):

- All modified SCB specimens were tested under load control to prevent damage to the CMOD and LLD gages.
- Based on the average time needed for the first test to reach 80% of the peak value, a loading rate of 0.9 kN/min was used.
- Before testing, all the samples were conditioned at the testing temperature for two hours.

- Each time the test ended with a "catastrophic" failure, and complete sample separation in two pieces in the notch plan. A chevron-notch geometry was not used. The fracture load was recorded.

The results are shown in Figure 5.6 and also presented in Table 5.2.

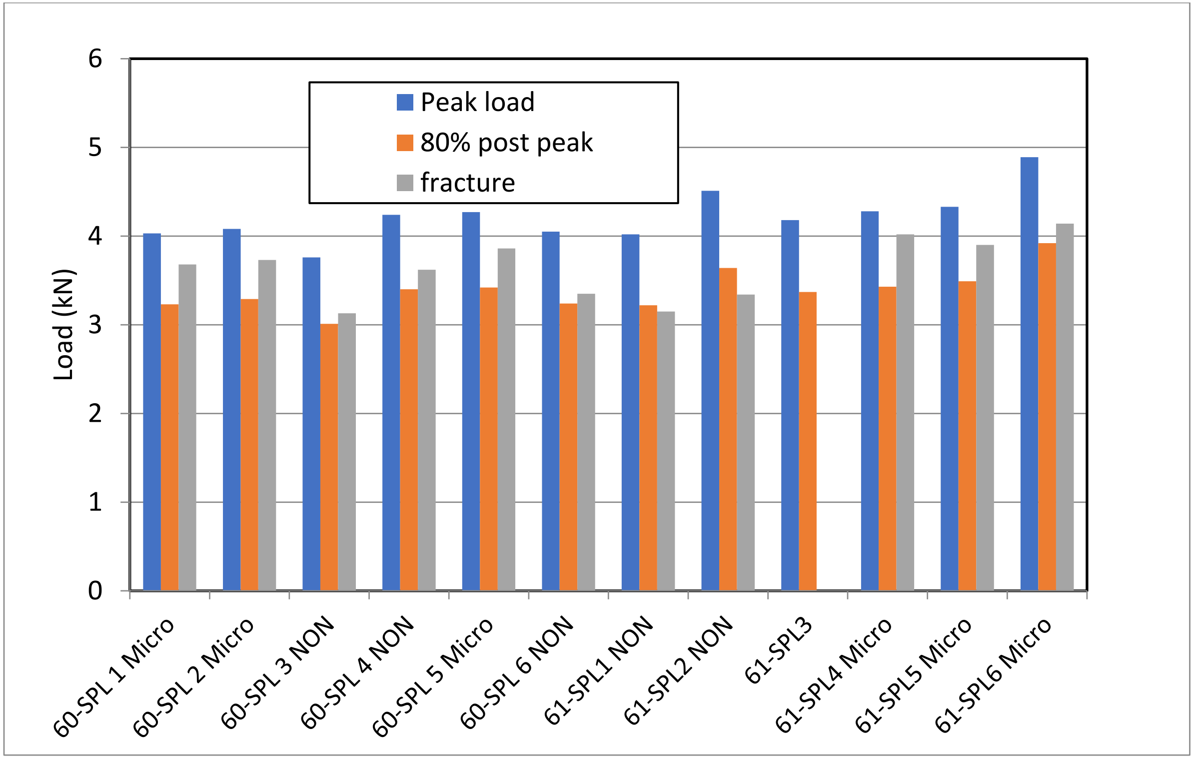

Figure 5.5: Comparison of peak loads, 80% post-peak loads, and final fracture loads.

Table 5.2: SCB Test Results.

Sample	First test, CMOD control			Treatment	Second test, Load control
	Peak Load	80% post-peak measured	0.8% peak calculated		Load at Fracture
60-SPL 1 Micro	4.03	3.23	3.22	Microwave	3.68
60-SPL 2 Micro	4.08	3.29	3.26	Microwave	3.73
60-SPL 3 NON	3.76	3.01	3.01	NON	3.13
60-SPL 4 NON	4.24	3.4	3.39	NON	3.62
60-SPL 5 Micro	4.27	3.42	3.42	Microwave	3.86
60-SPL 6 NON	4.05	3.24	3.24	NON	3.35
61-SPL1 NON	4.02	3.22	3.22	NON	3.15
61-SPL2 NON	4.51	3.64	3.61	NON	3.34
61-SPL3	4.18	3.37	3.34	DNF	
61-SPL4 Micro	4.28	3.43	3.42	Microwave	4.02
61-SPL5 Micro	4.33	3.49	3.46	Microwave	3.9
61-SPL6 Micro	4.89	3.92	3.91	Microwave	4.14

It can be seen from Figure 5.5 that, for the samples without treatment (NON), the fracture occurred at a load level very close to 80% from the peak load measured during the first test. The first test was stopped at this 80% level and the sample broke under the same load during the second test. The coefficient obtained by dividing the load at fracture by the 80% post-peak, (in Table 5.2) averaged for the five NON tests is equal to 1.006, and that means that no change in strength was noticed without a treatment, as shown in Table 5.3. This result is well expected, and it shows that the testing method has reliable results.

For the samples undergoing the microwave oven treatment (Microwave), a considerable increase in the fracture load during the second test is observed. The result obtained when averaging the Q value for these samples is equal to 1.125. That means that on average the load increased by 12% when the samples were microwaved.

Table 5.3: Fracture load to post-peak load ratios.

Sample	Treatment	Average Q Load at fracture /load at 80% post-peak
ALL 60 and 61 SPL Micro	Microwave	1.125
ALL 60 and 61 SPL NON	NON	1.006
ALL 60-SPL Micro	Microwave	1.133
ALL 60-SPL NON	NON	1.043
ALL 61-SPL Micro	Microwave	1.116
ALL 61-SPL NON	NON	0.95

It is seen that all group-60 and group-61 samples showed a similar trend of Q value in terms of the effect of microwave treatment. Additional information can be obtained from the individual test data, as shown in Figures 5.6 and 5.7. All individual results are shown in Annex 1. The dark grey line shows the first test, which followed the SCB protocol, and was stopped at 80% from the peak value, and the red line is the second test, in load control.

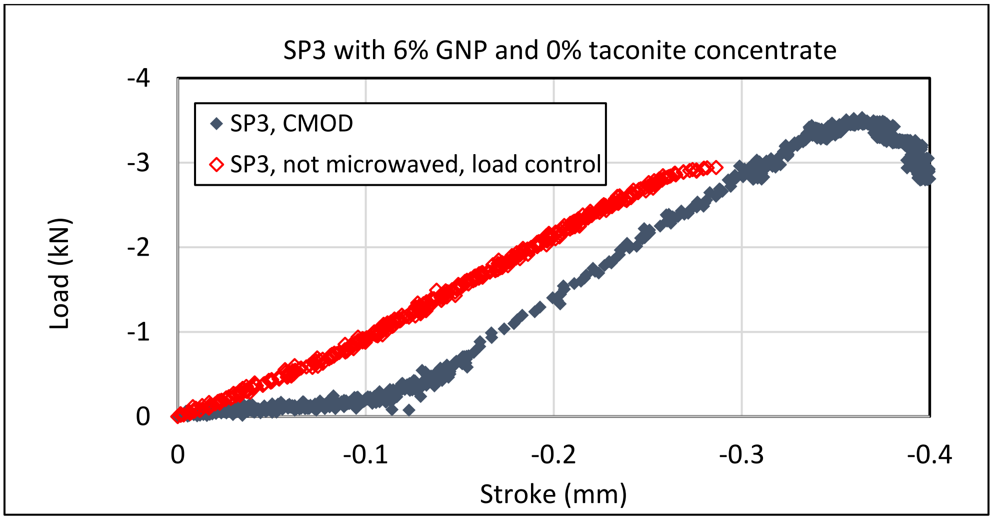

Figure 5.6: Experimental results on the mixture with 6% GNP not microwaved (NON).

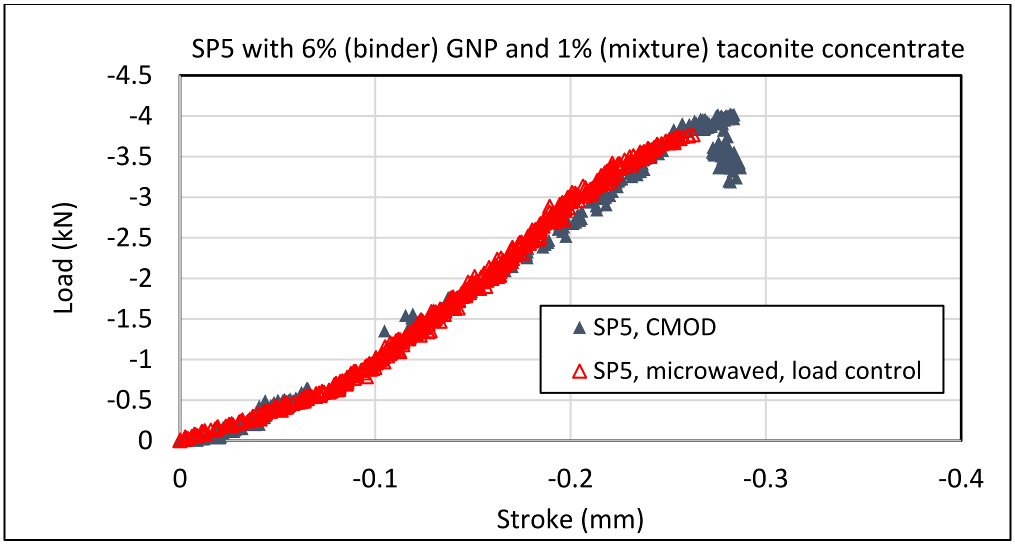

Figure 5.7: Experimental results on the mixture with 6% GNP and 1% taconite concentrate microwaved.

The comparison between Figure 5.7 and 5.8 leads to the following observations:

1) For NON specimens, the stiffness in the reloading phase is smaller than that in the initial loading phase. This indicates that, at 80% post-peak, the specimen experiences a considerable level of macroscopic damage in the form of a fully developed fracture process zone and possibly macrocrack propagation. Such damage is irreversible. In the reloading phase, the specimen fails at the load similar to the original 80% post-peak load.
2) For microwave treated specimens, the stiffness in the reloading phase is the same as that in the initial loading phase. The recovery of elastic stiffness indicates that the microwave heating led to damage healing. Meanwhile, in the reloading phase, the specimen attains a peak load that is slightly lower than the initial peak load of the original specimen. This further indicates the effectiveness of damage healing.

Based on the foregoing discussion, it is clear that the microwave heating on GNP- and CONC-modified specimen can lead to effective damage healing of macroscopic damage. The heated specimen could attain the original stiffness, and the strength can almost be recovered. Further investigation could focus on the optimization of the heating process (e.g. cyclic heating, heating duration), as well as the extension to the in-situ pavement by using a specially designed microwave-heating device.

CHAPTER 6: INVESTIGATION OF A MICROWAVE-BASED TACK COAT SYSTEM TO ENHANCE INTERLAYER BONDING

An investigation was performed to determine whether interlayer bonding can be enhanced by exposing a GNP-taconite modified tack coat material to microwave energy. In current construction practice, it is assumed that pavement layers are fully bonded into one integral unit. However, this assumption most of the time is not valid due to construction issues and the quality of bonding materials used. A poor bond can result in many different pavement distresses that decrease the pavement structural strength and life, ranging from top-down cracking, potholes, and fatigue failure. Shear strength testing of the bond between two asphalt specimens, some bonded with normal tack coat, and some with tack coat modified with GNP and taconite concentrate, that were also microwaved before testing, were performed and the results were compared.

6.1 SPECIMEN PREPARATION

In this investigation, 24 test specimens were fabricated and tested. Each specimen consists of two asphalt pucks bonded with a tack coat layer. For half of the specimens, a plain tack coat was used. For the other half, the tack coat was modified with a mixture of GNP and taconite concentrate, and the specimens were also heated using microwave energy before performing the shear test. The asphalt material used in the preparation of all specimens was loose asphalt mixture from Hennepin County Road 61 project.

First, the pucks representing the bottom part of the test specimens were prepared. The loose mix was heated to 135°C and then compacted at 60 gyrations using a Superpave Gyratory Compactor (SGC). Each puck had a diameter of 6 in and was 2.1in tall. The pucks were allowed to cool to room temperature and then tack coat was applied to the top face of each puck.

In this investigation, SAP 005-606-020 CSS-01 tack coat material was used. The material was diluted to seven parts emulsion and three parts water, as recommended by the supplier. According to Table 2357-2 from the 2018 Minnesota specification book, if new asphalt and (7:3) diluted tack coat are used, a range of 0.06-0.09 gal/yd^2 (0.27-0.41 L/m^2) of tack coat is acceptable (MnDOT, 2018). Given that each core had a diameter of 150mm and a face surface area of 0.01767m^2, the acceptable tack coat range per core was calculated to be 4.8 to 7.2mL. For all pucks, 6mL of tack coat solution was used.

First, the solution was heated to 100°F (37°C), based on the recommendations from MN 2018 standard Specification, section 2357.3 paragraph E. After shaking vigorously, a syringe was used to apply the tack coat to the upper face of each puck in straight lines, followed by passing a natural bristle brush to evenly spread the tack across the face. A sponge brush was then used to remove excess moisture and ensure an even coat. Examples of pucks with applied tack coats are shown in Figure 6.1. The tack coat was allowed to cure for 30 minutes before the second compaction was performed.

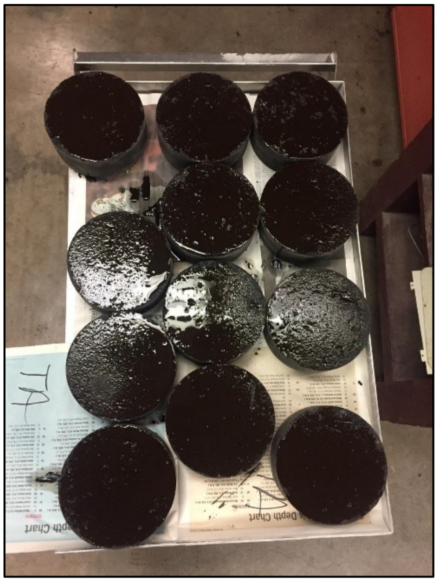

Figure 6.1: Bottom pucks with applied tack coat.

For the tack coat modified with GNP and taconite concentrate (GNPC), a mixture of GNP and concentrate was added to the tack coat layer before second compaction. After the tack coat was applied, for half of the puck, 0.36g of GNP and 0.36g of taconite concentrate were added for each puck. These quantities represent 6% of the tack coat weight. The GNP and taconite concentrate blend was added directly to the tack coat surface and a tool was used to spread it out evenly. This procedure allowed for better control of the quantities used for each puck. The tack was allowed to cure for 30 minutes before performing the second compaction.

The upper part of the shear test specimens was prepared using a second compaction. First, the SGC mold was reheated and the bottom puck was placed inside with the tack coat face up. The same amount of loose mix used to create the bottom puck was heated to 135°C and placed in the mold directly on top of the bottom puck. The loose mix was then compacted at 60 gyrations. This procedure reasonably follows the procedure used in field applications. Using this method, 24 shear test specimens were fabricated; 12 have the normal tack coat (TA) and 12 have the tack coat modified with GNP and taconite concentrate (GNPC).

6.2 MICROWAVE EXPERIMENTS

Before performing the bond shear testing, the GNPC specimens were exposed to microwave energy to determine if this procedure improves bonding strength. To better evaluate the microwave energy absorption of the modified tack coat layers, all microwave experiments were performed at NRRI, where researchers have access to specialized equipment. After the specimens were prepared at UMN, all 12 GNPC specimens and 3 of the 12 TA specimens were transported to Duluth for microwave oven treatment. The remaining 9 TA specimens were kept at the UMN laboratory.

The 3 TA specimens and 3 of the 12 GNPC specimens were used for energy absorption and temperature experiments at the NRRI laboratory. Preliminary microwave heating tests were conducted between October and December to confirm the proposed experimental procedure. Figure 6.2a illustrates conceptually how an asphalt specimen was configured and used to evaluate heating duration times and the potential variation of temperature measurement depending on thermocouple location and depth. A wooden jig was fabricated to hold the asphalt specimens steady while the thermocouple holes were drilled (Figure 6.2b-c). Thermocouple holes were drilled using a percussion drill fitted with a carbide-tipped masonry bit.

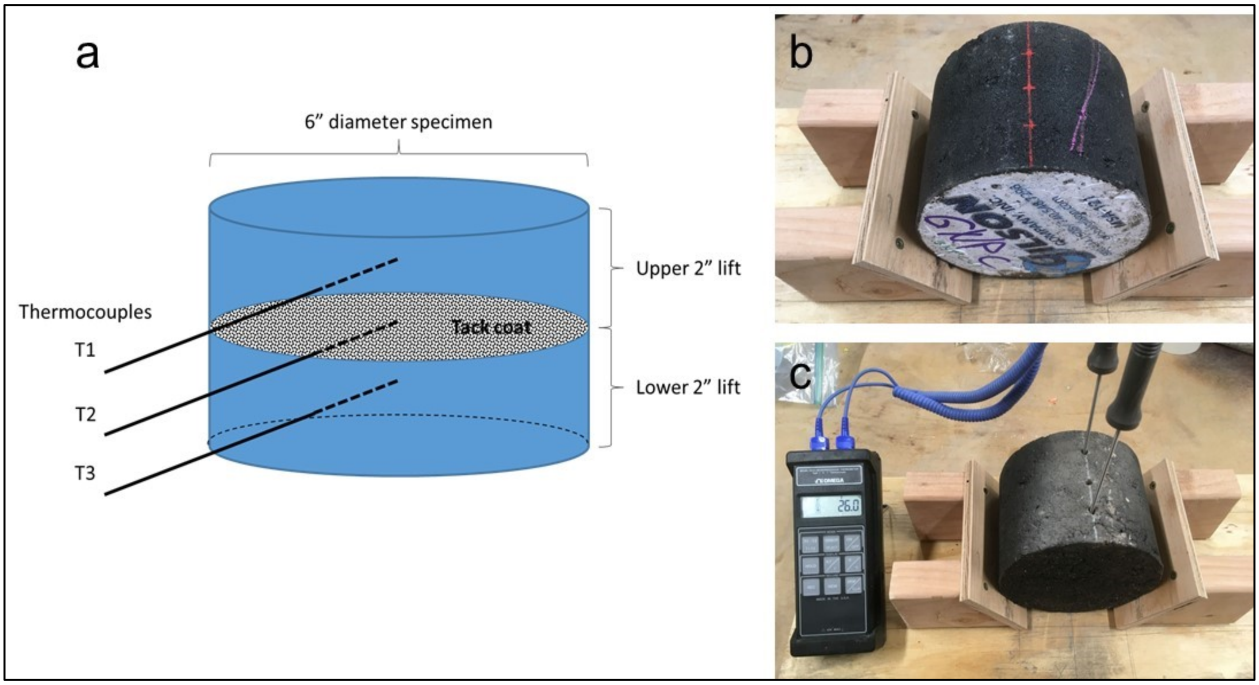

Figure 6.2: Specimen setup for determining microwave heating duration: (a) Diagram of the specimen, (b) Specimen held by wooden jigs, (c) Specimen voltage being read

Based on the preliminary testing results, nine (9) GNP-C specimens were microwave-treated on January 5, 2021, for exactly 15 minutes each to achieve a minimum internal temperature of 60°C using a common procedure, as described below.

Each GNPC specimen was placed on top of a metal sheet and under the cone of a custom-built 1kW, 2450MHz microwave device, as shown in Figure 6.3a-b. The metal sheet ensured that all of the microwave energy would be absorbed by the specimens and not by the material or substrate below the specimen. Test specimens are shown in front of the device. Each specimen was heated for 15 min until reaching a temperature of 55-65°C. A FLIR Systems InfraCAM™ thermal imaging camera borrowed from UMD’s Department of Mechanical and Industrial Engineering was used to visually document the nature of the microwave heating and provide supplemental temperature information. An example of this can be seen in Figure 6.4. The starting and ending temperatures of the top and bottom of each specimen were recorded (Table 6.1). The specimens were numbered and transported back to UMN for tack coat bond shear strength testing.

(a) (b)

Figure 6.3: Microwave setup used to heat the GNPC specimens: (a) full setup and (b) close-up

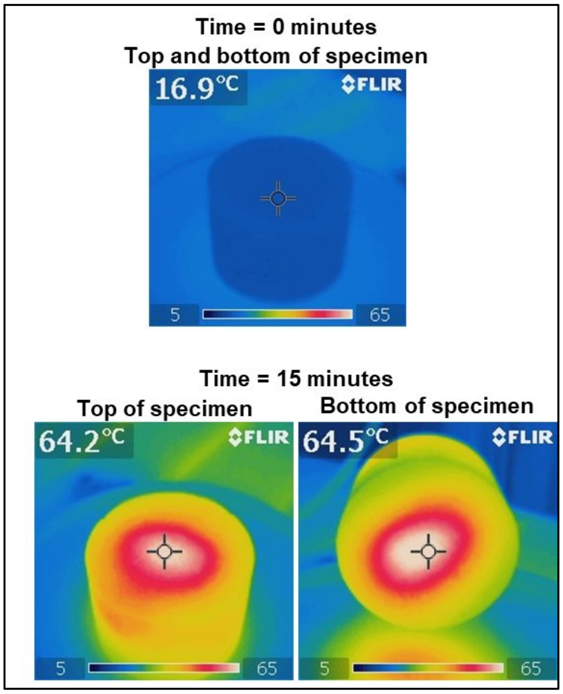

Figure 6.4: Pre- and post-microwaved thermal images of the specimen.

Table 6.1: 15-minute heating record of nine GNPC specimens, January 5, 2021.

Specimen	Time Start	Time End	Starting Temp (°C) Top	Starting Temp (°C) Bottom	Ending Temp (°C) Top	Ending Temp (°C) Bottom
1	11:19	11:34	12	12	70	60
2	11:40	11:55	14.5	14.5	71	58
3	12:02	12:17	15.5	15.5	67	63
4	12:24	12:39	16	16	75	67
5	12:48	13:03	17	17	64.5	64.5
6	13:41	13:56	19	18.5	85	78
7	14:04	14:19	18	18	73	74
8	14:25	14:40	18	18	67	78
9	14:48	15:03	18.5	18.5	72	79

6.3 TACK BOND SHEAR STRENGTH TESTING

For this experimental work, an MS-43 Asphalt Tack Bond Shear Strength Apparatus was used. This device is similar to the one used by Ozer and Rivera-Perez in their investigation of tack coat materials (Ozer & Rivera-Perez, 2017), and it is shown in Figure 6.5. While this simple apparatus does not provide accurate control of normal forces, it provides a very simple approach to obtain reliable data for proof-of-concept research.

Figure 6.5: MS-43 Asphalt Tack Bond Shear Strength Apparatus

The device consists of a frame that is split into two sides. One side is fixed (reaction frame) and holds the bottom of the specimens. The other side moves according to a shear load stroke actuator (loading frame) and holds the top of the specimen. The two sides of the frame are separate and can move independently. While a constant normal force can be applied to the specimen using a calibrated spring, for simplicity, no additional normal force was applied to the specimens during the tests run in this study.

Nine TA specimens and nine GNPC specimens were tested using an identical procedure that followed closely ASTM Standard TP 114-18. (AASHTO, 2019). For each type of tack coat, three specimens were tested at room temperature (20°C), three were tested at "refrigerator" temperature (4°C), and one was tested at "freezer" temperature (-18°C).

Since the MS-43 apparatus did not fit in the existing environmental chamber used with the MTS servo-hydraulic machine, a different approach was used to condition the specimens. First, the environmental chamber was removed, and the bonding strength fixture was installed on the MTS frame. The specimens were conditioned overnight at the specified temperatures and then were removed and quickly placed in the test device and tested. The process of removing the specimens from their conditioning environment, installing them into the MS-43 apparatus, and beginning testing did not take more than 2min, and therefore, it can be reasonably assumed that the temperatures of the specimens did not significantly change during testing.

The specimens were placed in MS-43 apparatus so that the tack coat interface was located in the middle of the gap between the loading and reaction frames. During testing, the shear load stroke actuator produced a uniform vertical movement of 0.1in/min until failure. The movement of the loading frame and the axial force applied to the specimen was continuously measured during testing, and the maximum shear stress was calculated. All specimens conditioned at 20°C and 4°C failed along the tack coat interface. An example of a failed specimen can be seen in Figure 6.6. for each specimen that was tested.

Figure 6.6: A specimen that failed along the tack coat interface.

For the first specimens conditioned at -18°C, failure did not occur in the tack coat interface. Also, the loading required was at the upper limit and no additional tests were performed to avoid possible damaging the laboratory equipment.

6.4 EXPERIMENTAL RESULTS AND DISCUSSION

Plots of shear stress vs. axial displacement for each of the tested specimens are shown in Figures 6.7 through 6.12. In the figure legend, each GNPC specimen has an ID of "mw#", and each TA specimen has an ID of "nmw#". It can be noticed that the plots for specimens nmw5 and nmw6 in the TA refrigerator grouping were flattened. It was found that the nut on the loading cell began to deform, and therefore, the plastic deformation of the nut was responsible. Once this was discovered, the nut was replaced. Please note that this did not affect the maximum shear load and stress.

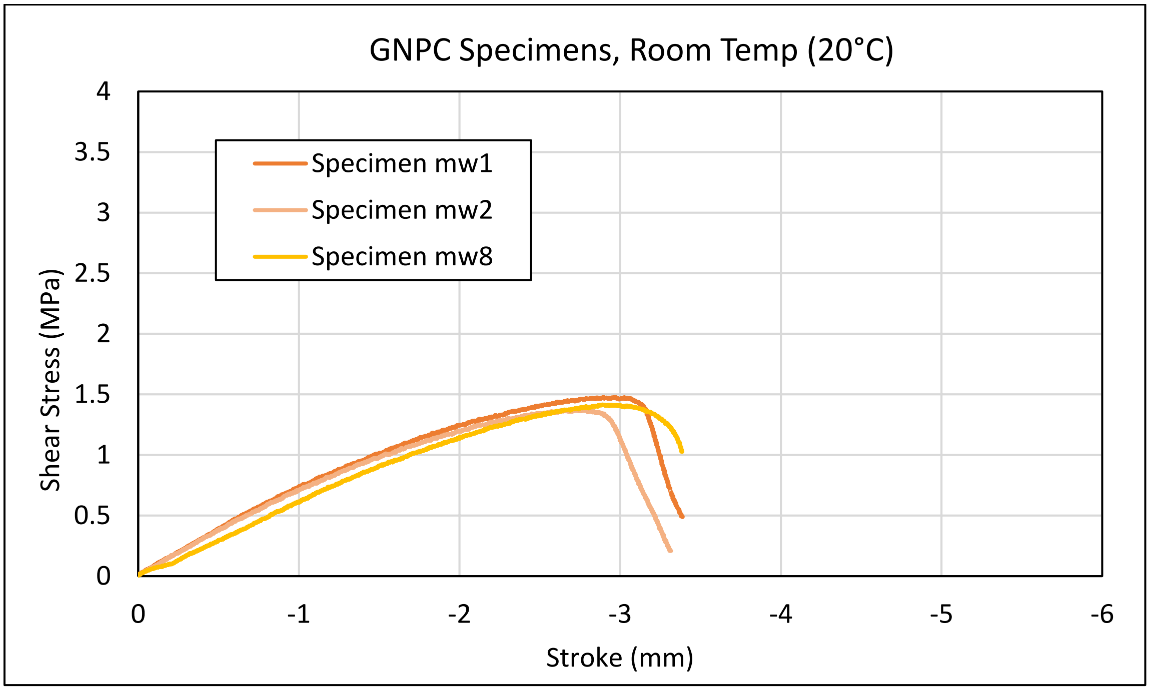

Figure 6.7: Results of the GNPC specimen tack coat shear strength tests at room temperature.

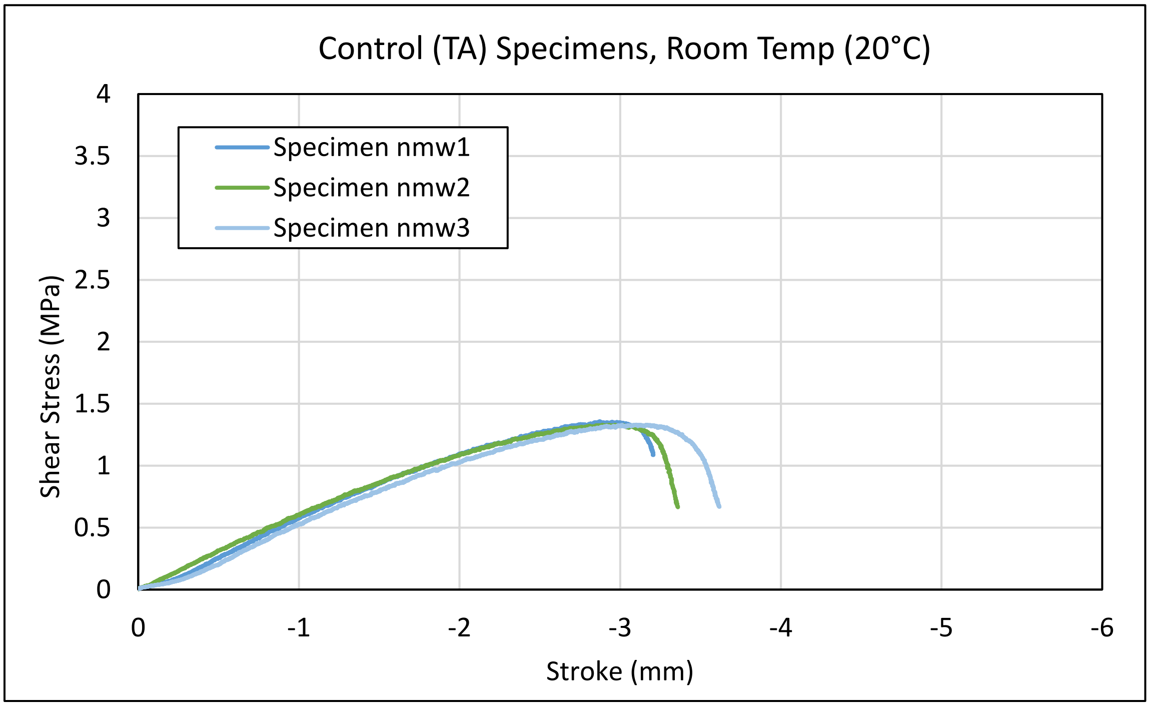

Figure 6.8: Results of the control specimen tack coat shear strength tests at room temperature.

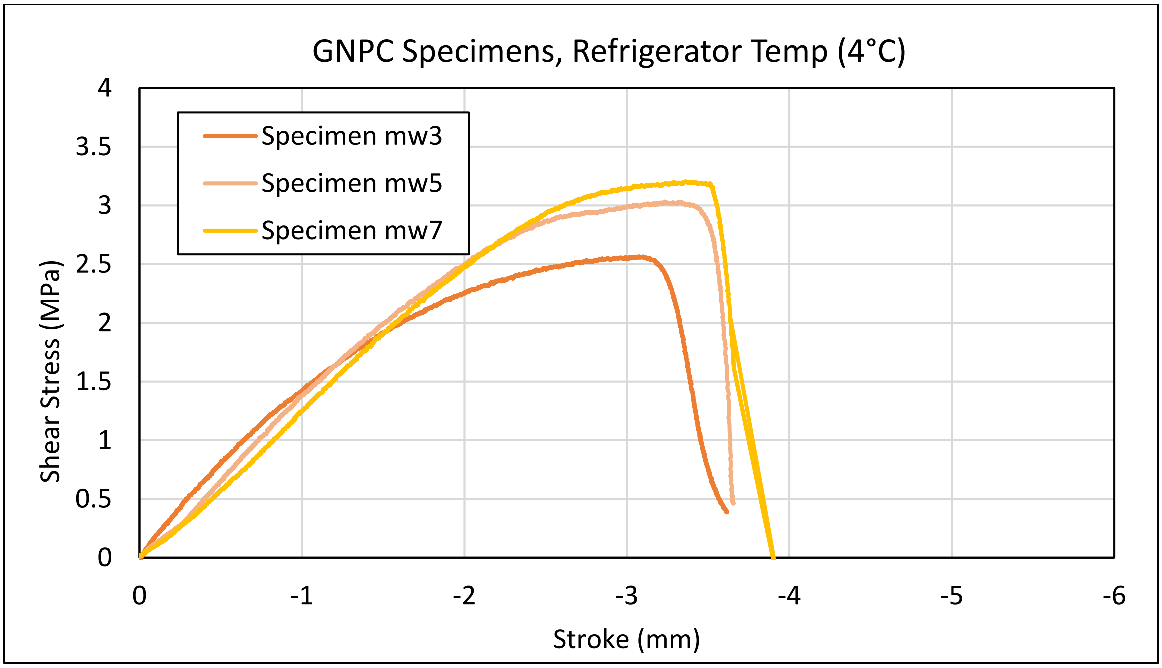

Figure 6.9: Results of the GNPC specimen tack coat shear strength tests at refrigerator temperature.

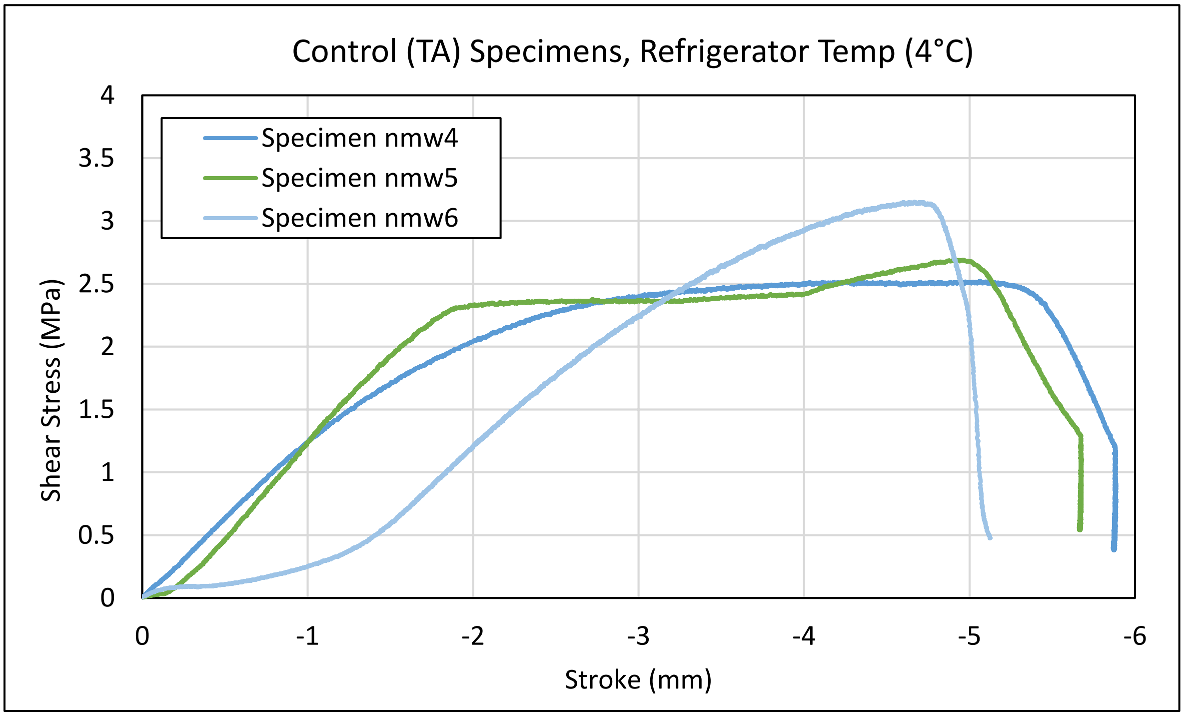

Figure 6.10: Results of the control specimen tack coat shear strength tests at refrigerator temperature.

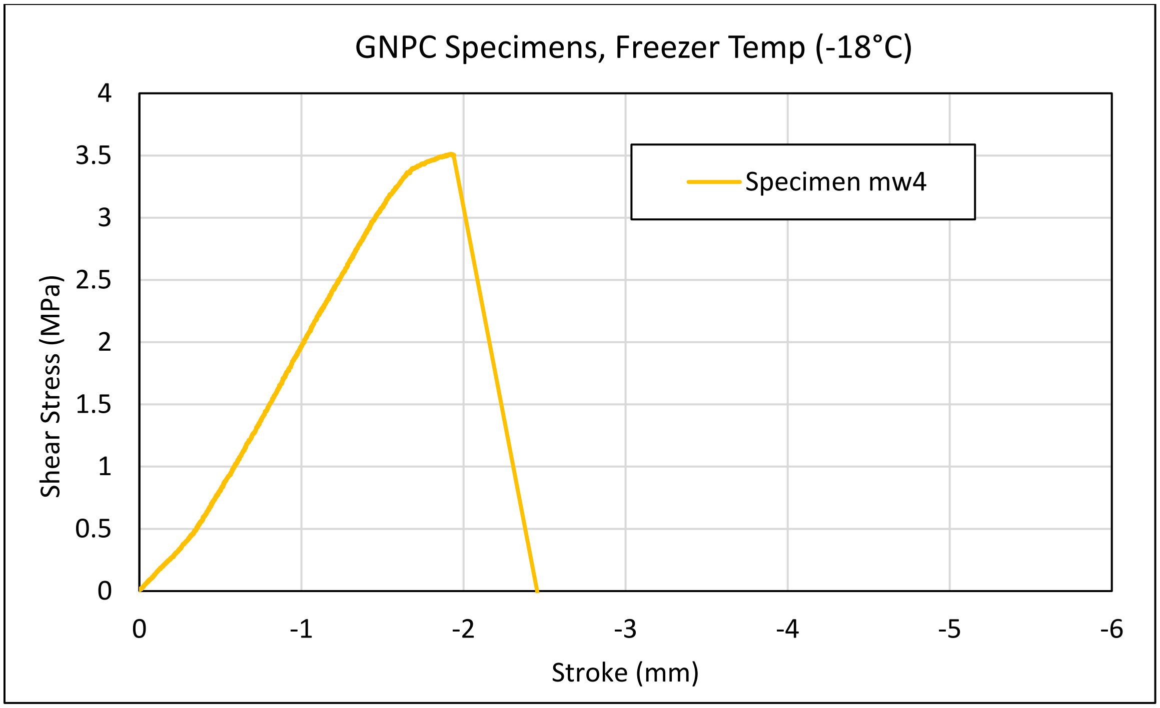

Figure 6.11: Results of the GNPC specimen tack coat shear strength tests at freezer temperature.

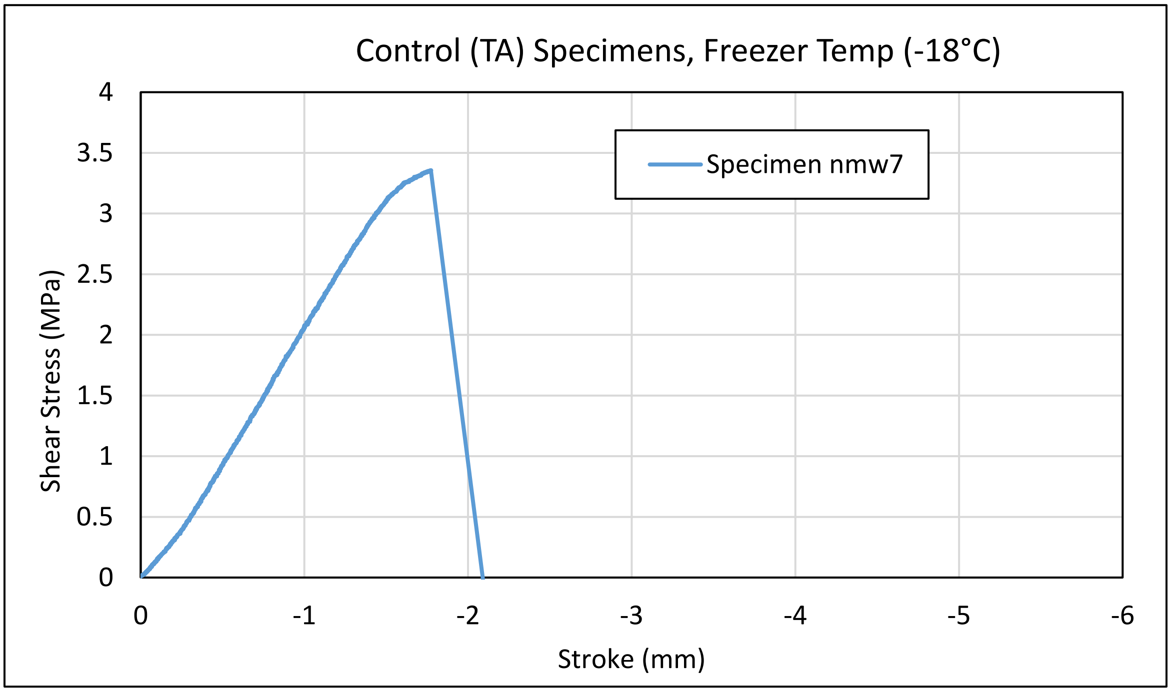

Figure 6.12: Results of the control specimen tack coat shear strength tests at freezer temperature.

The maximum shear stress was calculated for each test. The average max shear stress and standard deviations for each temperature grouping within each set are shown in Table 6.2. The results are also shown in Figure 6.13.

Table 6.2: Average max shear stress and standard deviation

	Average Max Shear Stress (MPa)		Std Dev Max Shear Stress (MPa)	
	GNPC	Control (TA)	GNPC	Control (TA)
Test at 20°C	1.42	1.34	0.042	0.012
Test at 4°C	2.93	2.79	0.27	0.266
Test at -18°C	3.51	3.36	0	0

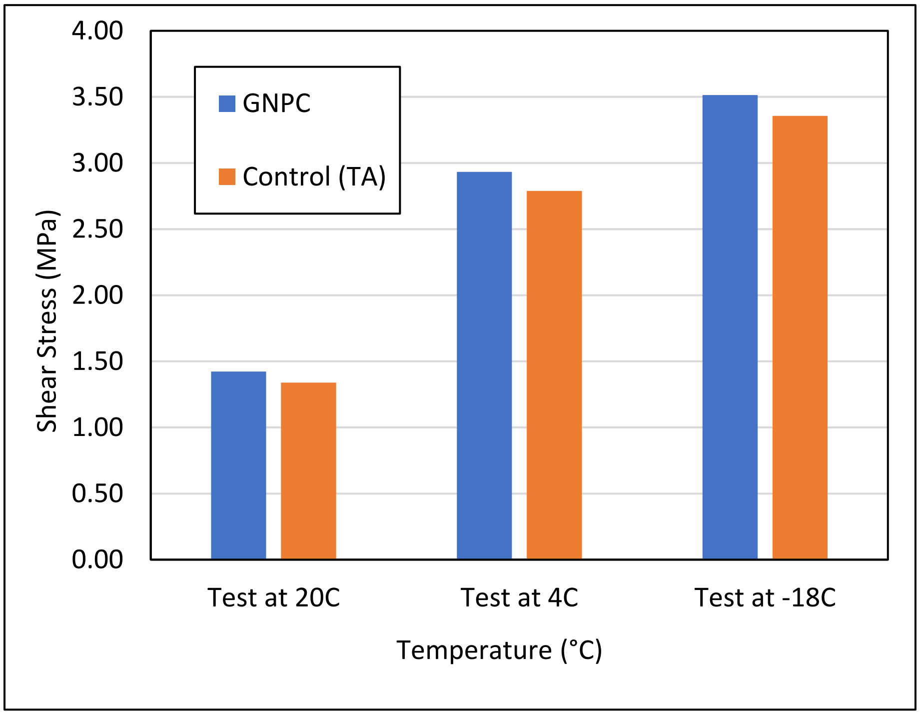

Figure 6.13: Average of the max shear stress readings for tests within each temperature grouping in the two sets.

The GNPC specimens show a 5.97% increase in shear strength at 20°C and a 5.02% increase at 4°C. Because the failure of the -18°C tests did not occur at the tack coat interface, no conclusions on the strength of the tack coat can be made from them. Although the GNPC specimens showed increased tack coat shear strength, the coefficient of variation (CoV) for those specimens was ~3.3 times that of the control specimens at room temperature. They were roughly the same in that regard at refrigerator temperatures. It should be mentioned that the limited number of test specimens may not be sufficient for evaluating the CoV. Nevertheless, the test result indicates that the shear strength of GNPC specimens exhibits more randomness. The random behavior of GNPC specimens could be caused by some non-uniformity of the properties of the GNPC tack coat. Therefore, how to effectively mix GNPC with tack coat requires future investigation.

CHAPTER 7: RESEARCH BENEFITS AND IMPLEMENTATION STEPS

This task clarifies and documents the methodology used to calculate benefits, including any assumptions and steps required. The tasks also include the key steps to implement the results of the research performed in this study.

7.1 RESEARCH BENEFITS

During the proposal phase, reduced life cycle cost was selected to define the benefits that the state will receive from the results and conclusions of this research, as shown in Table 7.1.

Table 7.1: Key expected benefits

Benefit Category	Key categories applicable to this project	Are the benefits quantifiable (Yes/No)	How will these benefits be quantified?
Material Cost Savings			
Decrease Engineering/ Administrative Costs			
Reduce Road User Costs			
Construction Savings			
Reduce Lifecycle Costs	X	Yes	Perform LCCA
Reduce Environmental Impact	X	No	
Improved Safety			
Operation and Maintenance Saving			
Reduce Risk			

As already mentioned, early detection of damage and cracking and timely repair is essential for extending the lifespan of the pavements. Each dollar spent in the early-stage of pavement life could eliminate or delay spending \$6 to \$10 in future rehabilitation or reconstruction costs.

In Tasks 3 and 4, experimental work and analyses were performed to determine if a novel asphalt material, in which GNP materials, taconite concentrate, and conventional asphalt binders are combined, can be used for sensing damage. The extent of damage is assessed by periodic measurements of the electrical resistance of the pavement. Although the results were positive, the significant effect of moisture on the electrical resistance measurements makes this technology less promising for early detection in field applications, where the moisture condition of the pavement changes periodically and extensive calibration is needed.

However, as clearly shown in Task 5, the healing potential of this novel material is significant. Application of microwave energy to partially damaged (cracked specimens) restores the condition of the material prior to damage, which represents a very good indication of the increase in durability.

To approximately quantify the benefits of such an improvement, a simple life cycle cost calculation was performed for a given pavement structure and design life. This was done by following MnDOT procedures outlined in the MnDOT Pavement Design Manual (MnDOT 2016). Two spreadsheets, both developed by MnDOT were used. The first is designed to sum all initial construction costs for each potential road design being considered for a particular project. The second calculates the life cycle cost and requires the input of the initial estimate costs, then adds maintenance schedule costs for each design, outputting a summary that allows for comparison of all designs being considered.

For simplification, we considered the example of a mill and overlay scenario used as a control in a previous project on SFDR application on TH5 (Hartman et al. 2016). The pavement structure is shown in Figure 7.2, and the initial cost is shown in Table 7.2.

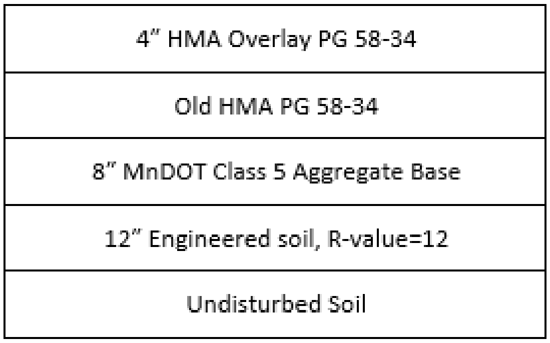

Figure 7.1: Control pavement structure for TH-5

Table 7.2: Initial costs for placement of one mile of mill and overlay (control)

Specification - Description	Depth (in)	Width (ft)	Quantity (mile)	Unit	Unit Price	Cost (mile)
2232501/00050 - MILL BITUMINOUS SURFACE (2.0")	2	40	23466.7	SY	$1.01	$23,679.17
2360501/23200 - TYPE SP 12.5 WEARING COURSE MIXTURE (3,B)	2	24	1591.0	TON	$56.99	$90,678.93
2360501/23200 - TYPE SP 12.5 WEARING COURSE MIXTURE (3,B)	1.5	40	1988.8	TON	$56.99	$113,348.67
2118501/00010 - AGGREGATE SURFACING CLASS 1	2	3	178.2	TON	$25.00	$4,455.00
					Cost/Mile:	**$232,161.77**

Year	Activity	Cost	Pres. Cost/per Mile
0	2" ML Mill & Fill and 1.5" Full width Overlay	$ 232,161.77	$ 232,161.77
1			$ -
2			$ -
3	Crack Treatment	$ 2,534.40	$ 2,417.97
4			$ -
5			$ -
6			$ -
7	Seal	$ 11,520.89	$ 10,323.54
8			$ -
9			$ -
10			$ -
11			$ -
12			$ -
13			$ -
14			$ -
15			$ -
16			$ -
17	ML Mill 3.5"	$ 233,196.02	$ 178,641.18
18			$ -
19			$ -
20	Crack Treatment	$ 2,534.40	$ 1,852.30
21			$ -
22			$ -
23			$ -
24	Seal	$ 11,520.89	$ 7,908.41
25			$ -
26			$ -
27			$ -
28			$ -
29			$ -
30			$ -
31			$ -
32			$ -
33	ML Mill 4.0"	$ 259,860.65	$ 154,906.50
34			$ -
35	15/17 Remaining Life	$ (229,288.81)	$ (132,463.30)
		Net present Cost / per mile	$ 455,748.37
		Equivalent Annual Cost	$ 17,052.00

Figure 7.2: Maintenance schedule for mill and overlay.

Year	Activity	Cost	Pres. Cost/per Mile
0	2" ML Mill & Fill and 1.5" Full width Overlay	$ 232,161.77	$ 232,161.77
1			$ -
2			$ -
3			$ -
4	Crack Treatment	$ 2,535.40	$ 2,381.30
5			$ -
6			$ -
7			$ -
8	Seal	$ 11,521.89	$ 10,163.85
9			$ -
10			$ -
11			$ -
12			$ -
13			$ -
14			$ -
15			$ -
16			$ -
17			$ -
18	ML Mill 3.5"	$ 233,197.02	$ 175,863.31
19			$ -
20			$ -
21	Crack Treatment	$ 2,535.40	$ 1,824.21
22			$ -
23			$ -
24			$ -
25	Seal	$ 11,521.89	$ 7,786.07
26			$ -
27			$ -
28			$ -
29			$ -
30			$ -
31			$ -
32			$ -
33			$ -
34	ML Mill 4.0"	$ 259,861.65	$ 152,497.63
35	16/17 Remaining Life	$ (244,575.67)	$ (141,294.73)
Net present Cost / per mile			$ 441,383.41
Equivalent Annual Cost			$ 16,514.53

Figure 7.3: Modified maintenance schedule for mill and overlay.

Once this information is input, a 35-year HMA maintenance schedule is automatically generated. Design life is specific to the pavement type and cannot be changed; for a mill and overlay design life is either 13-17 years or >17 years. Based on the design life of 17 years, the maintenance schedule for mill and overlay (control) was input and the initial estimate was entered into year 1. The schedule was automatically generated, as shown in Figure 7.3, and the equivalent uniform annual cost was calculated.

Since the information obtained in this project is limited to laboratory studies, we made the simplified assumption that the application of microwave energy and healing delays all maintenance and application of a new overlay schedule by 1 year. Based on this assumption, a new schedule is generated, and equivalent uniform annual costs are calculated, as shown in Figure 7.4.

The results are summarized in Figure 7.5, and as shown, the healing reduces the annual cost per mile for a 35-year period analysis by $537.

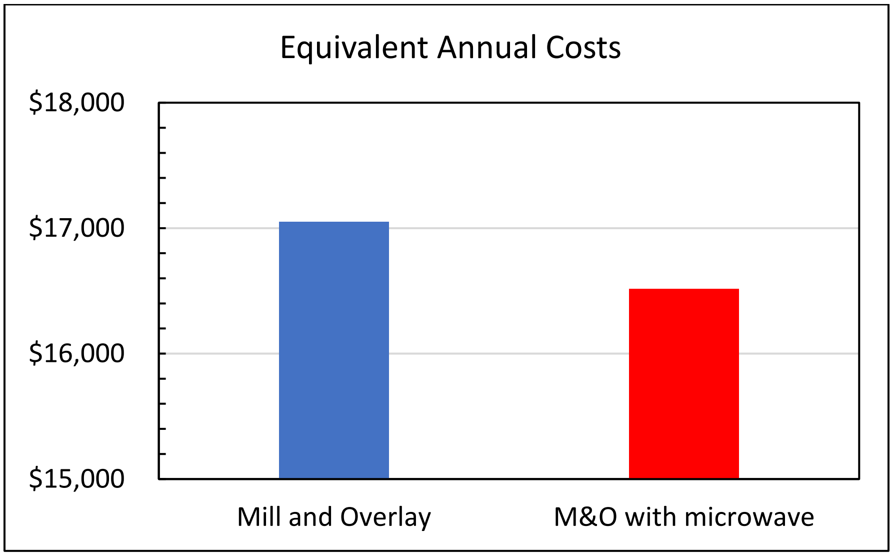

Figure 7.4: Comparison of annual equivalent costs over 35 years

7.2 IMPLEMENTATION STEPS

At the end of the proposed research, it is expected that new innovative materials will be developed, and current microwave technology will be further refined. The research team is currently working with the MnDOT Office of Materials and Research to identify funding mechanisms for building a test section at MnRoad. The section will be used to monitor the field performance of a pavement built with the new materials and microwave technology.

Once the field performance results become available and are positive, MnDOT can start implementing the use of these materials and technology for pavement preservation. The implementation process requires the active participation of asphalt mixture contractors to obtain critical industry feedback on the benefits and shortcomings of the new materials and technology.

CHAPTER 8: SUMMARY, CONCLUSION, AND RECOMMENDATIONS

In this research effort, we investigated the damage sensing and healing capability of a new class of asphalt materials – graphite nano-platelet (GNP)-taconite modified asphalt mixtures. The overarching goal was to develop an innovative asphalt material for efficient early damage detection and rehabilitation of pavement infrastructure. Through a comprehensive set of experiments as well as theoretical investigation of the concept of damage sensing, this research revealed the potential of the application of GNP-taconite modified asphalt mixtures for pavement rehabilitation.

First, we conducted a comprehensive literature review to document previous research efforts on modern techniques of non-destructive testing for asphalt pavements, which include ultrasonic, rolling density meters, laser scanning detection system, and digital image correlation. These methods rely on advanced devices, which sometimes are not easy to access. Furthermore, some of these methods, such as laser scanning detection and digital image correlation, are still limited to laboratory applications. Meanwhile, we also reviewed the modern view on pavement rehabilitation. It has been well acknowledged that early detection of pavement damage and timely repair will lead to significant savings in the life-cost of pavement infrastructure. The result of the literature review demonstrated the need for developing new ideas for damage detection and repair of asphalt pavements.

In Chapter 3, we experimentally investigated the electrical conductivity of GNP-taconite modified asphalt binders. A set of four-probe experiments was performed on specimens made of conventional binder, GNP modified asphalt binder, taconite modified asphalt binder, and GNP-taconite modified asphalt binder. The test results showed that, compared to the other mixes, the GNP-taconite modified asphalt binder exhibited the most significant improvement in electrical conductivity. It is believed that this improvement was attributed to the enhanced electron hopping mechanism.

In Chapter 4, we explored the theoretical model that relates the change of electrical conductivity and the extent of damage. The model was derived based on the fact that the electrostatic field is mathematically analogous to the elastostatic field under anti-plane shear loading. Leveraging this analogy, we used the formulation in fracture mechanics to obtain a closed-form relationship between the electrical conductivity and the material damage. In parallel with the theoretical model, a set of experiments was performed to investigate the effect of material damage on the electrical conductivity. It was shown that the humidity of the testing environment can have a strong influence on the measured electrical conductivity.

In Chapter 5, we investigated the damage healing capability of GNP-taconite modified asphalt binders through a two-stage experiment. In the first stage, the semi-circular bend specimen was loaded to the post-peak regime to introduce damage at the notch tip. The pre-damaged specimen underwent microwave treatment and was reloaded to the ultimate failure. It was observed that, after microwave treatment, the pre-damaged specimen was able to reach the load capacity of the original specimen, which signifies the effectiveness of damage healing.

In Chapter 6, we applied microwave technology to a tack coat system with a GNP-taconite asphalt interface. Experiments were first performed to determine the duration of microwave treatment to ensure the sufficient rise of temperature at the interface. The interfacial bond strength was measured by a direct shear device. The shear tests showed that, after microwaving, the GNP-taconite asphalt interface exhibited an improved bond strength.

The research performed as part of this study clearly demonstrated the potential benefits of using newer technologies and materials, such as microwave energy, for asphalt healing and for interlayer bonding enhancement. At the same time, it also identified some limitations, such as the use of new materials for sensing applications, which can be significantly affected by environmental conditions.

The work performed in this report was done in laboratory conditions. Therefore, to fully investigate the potential benefits of using these newer technologies and materials, we recommend a series of field trials. It is also recommended that a limited number of proof-of-concept field experiments be performed first at the MnROAD research facility before embarking on any large-scale investigations.

REFERENCES

AASHTO. (2019). *Standard method of test for determining the interlayer shear strength (ISS) of asphalt pavement layers*. Washington, DC: AASHTO.

Ajideh, H., Bahia, H., U., & Earthman, J. (2012). Scanning laser detection system used to measure propagation of fatigue damage of asphalt mixes. *Transportation Research Record: Journal of the Transportation Research Board*, *2296,* 135–143.

Bažant, Z. P., & Planas, J. (1998). *Fracture and size effect in concrete and other quasibrittle materials*. Boca Raton, FL: C.R.C.

Bueno, M., & Arraigada, M. (2016). Damage detection and artificial healing of asphalt concrete after trafficking with a load simulator*. Mechanics of Time-Dependent Materials, 20*, 265–279.

Chan, S., Lane, B., Kazmierowski, T., & Lee, W. (2011). Pavement preservation - A solution for Sustainability. *Transportation Research Record: Journal of the Transportation Research Board 2235,* 36-42.

Ghosh, D., Turos, M., Hartman, M., Milavitz, R., Le, J.-L., & Marasteanu, M. (2018). *Pothole prevention and innovative repair*. St. Paul, MN: Minnesota Department of Transportation Research Services & Library.

Hammond, P., J. (2013). *The gray notebook* (WSDOT's quarterly performance report on transportation systems, programs, and department management, 48). Olympia, WA: WSDOT.

Hartman, M., Turos, M., Gosh, D., & Marasteanu, M. O. (2016). *Full-depth reclamation (FDR) for suburban/urban and local road application*. St. Paul, MN: Minnesota Department of Transportation Research Services & Library.

Hoegh, K., Khazanovich, L., Maser, K., & Tran, N. (2012). Evaluation of ultrasonic technique for detecting delamination in asphalt pavements. *Transportation Research Record: Journal of the Transportation Research Board*, *2306,* 105–110.

Hoegh, K., & Dai, S. (2017). Asphalt pavement compaction assessment using ground penetrating radar-arrays. Paper presented at the Congress on Technical Advancement 2017, Duluth, Minnesota.

Khazanovich, L., Velasquez, R., & Nesvijski, E. G. (2005). Evaluation of top-down cracks in asphalt pavements by using a self-calibrating ultrasonic technique. *Transportation Research Record: Journal of the Transportation Research Board*, *1940,* 63–68.

Khripin, C., Jagota, A., & Hui, C. (2005). Electric fields in an electrolyte solution near a strip of fixed potential. *The Journal of Chemical Physics, 123*(13). doi:https://doi.org/10.1063/1.2043067

Kluthe, M. (2017). *Investigation of mixing procedure for graphite nano-platelets (GNP) reinforced asphalt binders* (Internship Opportunities Program). Minneapolis: Department of Civil, Environmental, and Geo- Engineering, University of Minnesota.

Le, J., Marasteanu, M., & Turos, M. (2016). *Graphene nanoplatelet (GNP) reinforced asphalt mixtures: A novel multifunctional pavement material* (The IDEA Program, NCHRP IDEA 173). Washington, DC: Transportation Research Board.

Le, J., Marasteanu, M. & Hendrickson, R. (2017). *A mechanistic design approach for graphite nanoplatelet (GNP) reinforced asphalt mixtures for low temperature applications*. St. Paul, MN: Minnesota Department of Transportation, Research Services & Library.

Li, M., Yang, M., Vargas, E., Neff, K., Vanli, A., & Liang, R. (2016). Analysis of variance on thickness and electrical conductivity measurements of carbon nanotube thin films. *Measurement Science and Technology, 27*(9). doi:10.1088/0957-0233/27/9/095004

Linden, R., N., Mahoney, J. P., & Jackson, N. C. (1989). Effect of compaction on asphalt concrete performance. *Transportation Research Record, 1217*,20-28.

McMeeking, R. M. (1990). A J-integral for the analysis of electrically induced mechanical stress at cracks in elastic dielectrics. *International Journal of Engineering Science, 28*(7), 605-613. doi:https://doi.org/10.1016/0020-7225(90)90089-2

MnDOT (2016). *MnDOT Pavement Design Manual.* St. Paul, MN: MnDOT

MnDOT (2018). *Minnesota Standard Specifications for Construction* (2018 Edition). Retrieved from https://www.dot.state.mn.us/pre-letting/spec/2018/2018-spec-book-final.pdf

Ozer, H., & Rivera-Perez, J. (2017). Evaluation of various tack coat materials using interface shear device and recommendations on a simplified device. Illinois Center for Transportation Seriese No. 17-027, Research Report No. FHWA-ICT-17-021, doi:10.36501/0197-9191/18-027.

Pellecuer, L., Assaf, G. J., & St-Jacques, M. (2014). Life cycle environmental benefits of pavement surface maintenance. *Canadian Journal of Civil Engineering*, 41(8), 695-702.

Saarenketo, T. (2006). Electrical properties of road materials and subgrade soils and the use of ground penetrating radar in traffic infrastructure surveys (Doctoral dissertation). Oulu, Finland: University of Oulu.

Suo, Z. (1993). Models for breakdown-resistant dielectric and ferroelectric ceramics. *Journal of the Mechanics and Physics of Solids, 41*(7), 1155-1176. doi:https://doi.org/10.1016/0022-5096(93)90088-W

Uhlmeyer, J., Luhr, D., Rydhom, T. (2016). *Pavement asset management*. Seattle: Washington Department of Transportation.